

Dynamic fracture of a bicontinuously nanostructured copolymer: A deep-learning analysis of *big-data-generating experiment*

Hanxun Jin, Rodney J. Clifton, Kyung-Suk Kim*

School of Engineering, Brown University, Providence, RI 02912, United States

* Corresponding author: kyung-suk_kim@brown.edu

Abstract:

Here, we report the dynamic fracture toughness as well as the cohesive parameters of a bicontinuously nanostructured copolymer, polyurea, under an extremely high crack-tip loading rate, from a deep-learning analysis of a dynamic *big-data-generating experiment*. We first invented a novel Dynamic Line-Image Shearing Interferometer (DL-ISI), which can generate the displacement-gradient - time profiles along a line on a sample's back surface projectively covering the crack initiation and growth process in a single plate impact experiment. Then, we proposed a convolutional neural network (CNN) based deep-learning framework that can inversely determine the accurate cohesive parameters from DL-ISI fringe images. Plate-impact experiments on a polyurea sample with a mid-plane crack have been performed, and the generated DL-ISI fringe image has been inpainted by a Conditional Generative Adversarial Networks (cGAN). For the first time, the dynamic cohesive parameters of polyurea have been successfully obtained by the pre-trained CNN architecture with the computational dataset, which is consistent with the correlation method and the linear fracture mechanics estimation. Apparent dynamic toughening is found in polyurea, where the cohesive strength is found to be nearly three times higher than the spall strength under the symmetric impact with the same impact speed. These experimental results fill the gap in the current understanding of copolymer's cooperative-failure strength under extreme

local loading conditions near the crack tip. This experiment also demonstrates the advantages of *big-data-generating experiments*, which combine innovative high-throughput experimental techniques with state-of-the-art machine learning algorithms.

Keywords:

- (1) dynamic fracture
- (2) *big-data-generating experiment*
- (3) nanostructured copolymer
- (4) deep learning
- (5) Dynamic Line-Image Shearing Interferometer (DL-ISI)
- (6) cohesive zone

1 Introduction

Recently, researchers have gained substantial interest in a nanophase-segmented block copolymer, polyurea, on its nanoscale dynamic toughening mechanisms (Clifton and Jiao, 2015; Grujicic et al., 2015; Jain et al., 2013; Youssef and Gupta, 2012). During the linear polymerization, thermodynamic incompatibility between the polytetramethylene oxide and diisocyanate enables the unique dual-phase bicontinuous nanostructures consisting of hard gyroid arms dispersed in a continuous soft medium, as observed in Atomic Force Microscopy (AFM) tapping-mode phase images (Das et al., 2007; Grujicic et al., 2014; Kim et al., 2020; Wisse et al., 2006). These bicontinuously segregated nanostructures are believed to provide dynamic deformation mechanisms responsible for the ultra-high strength of polyurea under extremely high strain-rate loading. For studying the dynamic failure response of polyurea, release-wave plate-impact experiments (Clifton and Jiao, 2015) were conducted. These experiments revealed tensile dynamic-failure-initiation stress of polyurea PU1000 is approximately 105 MPa under the uniaxial strain loading condition. However, polyurea did not directly spall within the duration of tensile-wave loading. Instead, micron-size voids were observed on the “spall plane”, continuing to transmit stress. Understanding the entire dynamic failure process in the spalling test requires accurate fracture models consisting of void initiation-growth-coalescence processes. Developing such high-fidelity cohesive models requires well-characterized dynamic fracture experiments rather than the “spall” tests. Such experiments, involving plane wave loading of samples with a mid-plane crack, have been previously invented and used to study the dynamic crack growth processes in AISI 4340 steel, under mode I (Ravichandran and Clifton, 1989) as well as modes II & III loading conditions (Zhang and Clifton, 2003, 2007). A schematic of the mode I dynamic fracture testing experiments using plate-impact loading is illustrated in **Fig. 1(a)**. Although the

dynamic mixed-mode cohesive properties of a dissimilar material interface could be measured in general with our methods, we focused on mode I fracture of polyurea, i.e., materials A and B in **Fig. 1(a)** are the same polyurea in this paper.

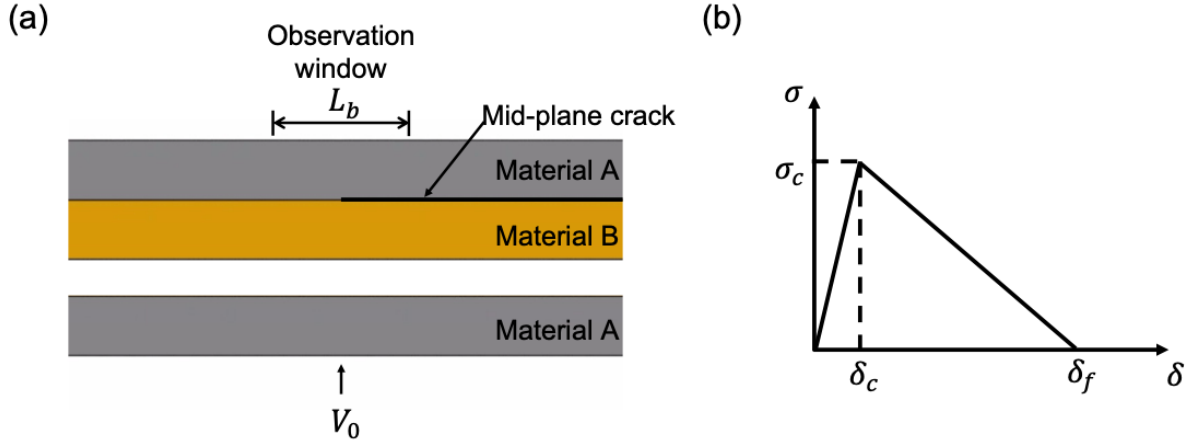


Figure 1 (a) A schematic of dynamic fracture testing using plate-impact loading: a flyer with initial speed V_0 is impacting a sample with a mid-plane crack. (b) The schematics of a bilinear cohesive law with three cohesive parameters ($\sigma_c, \delta_c, \delta_f$).

Failure processes are often characterized by cohesive zone models (CZM) (Barenblatt, 1983; Dugdale, 1960; Tvergaard and Hutchinson, 1996; Xu and Needleman, 1993) that provide a computational foundation for modeling failure in elastomers. In general, CZM employs a physical traction-separation law to describe the cohesive behavior between similar or dissimilar interfaces. For example, a simple bilinear cohesive law is illustrated in **Fig. 1(b)**. Since its development, CZM has been successfully used to describe various fracture and friction problems such as void growth in metals (Tvergaard and Hutchinson, 1996), polymer crazing (Hong et al., 2009; Hong and Kim, 2003), and single and multi-asperity friction (Kim et al., 1998; Li and Kim, 2008, 2009). Determining cohesive laws from experimental data is a nontrivial inverse problem. Practically,

experimentalists first measure the load-displacement curves at the boundary of a specimen (Bazant, 2002) or obtain the whole deformation field using optical methods such as moiré interferometry (Mohammed and Liechti, 2000). Then, optimization algorithms like the steepest descent method are employed to find the optimal cohesive parameters iteratively. However, using this approach to obtain accurate cohesive parameters is challenging. The non-uniqueness of the inverse problem may lead to finding parameters in local minima, which can also depend on the optimization algorithms.

Recent advances in machine learning, especially deep learning, provide a powerful method to solve inverse problems in engineering and physics (Hsu et al., 2020; Sanchez-Lengeling and Aspuru-Guzik, 2018; Shi et al., 2020; Zhang et al., 2020). In principle, the deep-learning approach uses a multi-layer neural network structure that can learn the nonlinear mapping between training dataset and pre-set labels or parameters (LeCun et al., 2015). Then, the pre-trained neural network can effectively predict parameters for the test dataset. Regarding using deep learning to determine the cohesive laws inversely, recent studies (Ferdousi et al., 2021; Su et al., 2021) have used load-displacement curves at the boundary of the specimen to train a deep dense-layer neural-net architecture. However, such a quasi-static load-displacement measurement technique cannot be applied to dynamic experiments under extreme conditions like plate-impact experiments where local strain rates exceed $10^6 s^{-1}$. At most, a laser interferometry technique like Normal Displacement Interferometry (NDI) or Transverse Displacement Interferometry (TDI) (Kim et al., 1977) was used to measure a time trace of displacements at a point to inversely determine the fracture toughness (Ravichandran and Clifton, 1989) based on analytical linear-elastic dynamic crack-tip solutions of Freund (Freund, 1972, 1973). However, such “one-point” measurement cannot accurately determine the interfacial properties like cohesive parameters. A new

experimental technique that can generate a sufficient dataset in a single experiment is desired for deep learning to determine the cohesive parameters inversely. We defined such a high-throughput experiment as a *big-data-generating experiment*. Such measurement can be readily achieved from our novel invention of the Dynamic Line-Image Shearing Interferometer (DL-ISI) with a high-speed streak camera system.

In this paper, we first present our invention of the Dynamic Line-Image Shearing Interferometer (DL-ISI) with the streak camera system in **Section 2**, which can record displacement-gradient - time information along a line on the specimen surface for material characterization. Then, we proposed a deep-learning framework that can inversely determine the accurate cohesive parameters in dynamic *big-data-generating experiments* in **Section 3**. Next, detailed plate-impact experiments on polyurea with mid-plane crack are discussed in **Section 4**. The experimental fringe image collected by the streak camera is cleaned and inpainted by a state-of-the-art Conditional Generative Adversarial Network (cGAN). The dynamic cohesive parameters and fracture toughness are then readily determined from the correlation method as well as the deep learning framework. The underlying molecular-level dynamic toughening mechanisms of polyurea will be presented in our sequel paper (Jin et al., 2021).

2 Dynamic Line-Image Shearing Interferometer (DL-ISI)

Due to the resolution limitation of the streak camera system, recording displacement profile directly using an interferometer like the Michelson type is challenging. The number of fringes obtained from the Michelson interferometer is $n = 2d/\lambda$, where d is the rear surface displacement, and λ is the wavelength of the laser. From a FEM analysis, d is estimated to be in the order of 1mm when the crack opens, and the fringe number n reaches approximately 4000, which is out of

the resolution of the streak camera system with 1024×1024 pixels. Therefore, a new interferometer that can measure the rear surface line profile with reasonable fringe density is needed. For this purpose, we invented the novel Dynamic Line-Image Shear Interferometer (DL-ISI), where the fringe information represents the rear surface's displacement gradients.

The DL-ISI optical design is shown schematically as black lines in **Fig. 2**. In the optical circuit, a laser beam with wavelength $\lambda = 532\text{nm}$ is controlled to synchronously switch the beam on by an acousto-optic modulator (AOM) (Brimrose TEM-110-5-532) located at the focal plane of the spherical lens SL1, for the exposure duration of a high dynamic range streak camera (Hamamatsu C7700). Then the laser beam is collimated and passing through a slit with a size of $10\text{mm} \times 2\text{mm}$. The slit of collimated beams is illuminated on the rear surface of the specimen with mirror-finish quality. The orientation of the illuminated slit is perpendicular to the crack-front line. Then, the reflected beam is projected on the image plane of the streak camera for one-to-one magnification imaging through the two spherical lenses SL2 and SL3 with the same focal length f_{len} . At the focal point of SL2, a microscope coverslip glass with $150\mu\text{m}$ thickness is used to create image shearing interfered fringes. The schematics of these two interfered beams reflected from the front surface and rear surface of the glass is shown in **Fig. 3**. The electric field of the beam reflected from the front surface of the glass and arriving at the image plane can be written as,

$$\mathbf{E}^{(1)}(x, y, z, t) = \mathbf{E}_0^{(1)} \exp \left\{ i \left[kz + \frac{k}{2R(z)} (x^2 + y^2) - 2ku(x, t) - \omega t \right] \right\}, \quad (1)$$

where (x, y) is the in-plane coordinate and z the light-propagation coordinate of the image plane, $R(z)$ is the radius of curvature of the wave front at z , and $R(z) = f_{len}$ at the image plane. Here, k and ω are the wavenumber and the angular frequency of the light, t the time, and $u(x, t)$ is the out-plane displacement of the sample. Since the slit height is much smaller than the width (less

than 1%), we consider the streak camera records the line displacement information only. The electric field amplitude of the beam reflected from the rear surface of the glass is,

$$\mathbf{E}^{(2)}(x + \Delta x, y, z', t)$$

$$= \mathbf{E}_0^{(2)} \exp \left\{ i \left[kz' + \frac{k}{2R(z')} ((x + \Delta x)^2 + y^2) - 2ku(x + \Delta x, t) - \omega t \right] \right\}, \quad (2)$$

where $z' = z + D + \beta z$ with D the optical path difference of these two beams in the glass and β is the angle between two reflected beams due to a small tilt angle α in the glass. Δx is the shearing distance in x direction. Their relation can be derived as,

$$D = 2h_g (n_g^2 - \sin^2 \theta_{in})^{1/2}, \quad (3a)$$

$$\Delta x = 2h_g \frac{\sin \theta_{in} \cos \theta_{in}}{\sqrt{n_g^2 - \sin^2 \theta_{in}}}, \quad (3b)$$

$$\beta = \frac{2\alpha (n_g^2 - \sin^2 \theta_{in})^{1/2}}{\cos \theta_{in}}, \quad (3c)$$

where h_g is the glass thickness, θ_{in} is the beam incident angle, and n_g is the refractive index of the glass. The intensity of these two interfered beams is,

$$I(x, y, z, t) = I_1 + I_2 + 2\sqrt{I_1 I_2} \cos(\phi), \quad (4)$$

where the phase difference ϕ is,

$$\phi = k \left\{ z + \frac{(x^2 + y^2)}{2R(z)} - 2u(x, t) - z' - \frac{[(x + \Delta x)^2 + y^2]}{2R(z')} + 2u(x + \Delta x, t) \right\}. \quad (5)$$

Since the distance from the glass to the image plane, z is 3 orders of magnitude larger than the optical path difference D , and the glass tilt angle α is measured as 0.018mrad which is considered as negligible, we consider $R(z) \cong R(z + D + \beta z)$. Assuming $I_1 \cong I_2 = I_0$, the intensity of these two interfered beams at the image plane can be derived as,

$$I(x, t) = 4I_0 \cos^2 \left(\frac{\phi}{2} \right) = 4I_0 \cos^2 \left\{ \frac{\pi}{\lambda} \left[D + \frac{\Delta x}{f_{len}} x - 2 \frac{\partial u(x, t)}{\partial x} \Delta x \right] \right\}. \quad (6)$$

As we can see from **Eq. 6**, the DL-ISI fringe variation depends on the displacement gradient along the image shearing direction $\frac{\partial u(x, t)}{\partial x}$. The second term represents an initial fringe density which caused by the shearing of the spherical wavefront at the glass plate. The number of initial fringes at the image plane of the streak camera is,

$$N_{inif} = \frac{L_b \Delta x}{f_{len} \lambda}, \quad (7)$$

where L_b is the slit width of the laser beam illuminated at the sample as shown in **Fig. 1(a)**. Our deep-learning analysis presented in **Section 3** shows that the optimum initial fringe density provides the most accurate cohesive-parameter determination. The initial fringe density can be controlled by the image shearing distance Δx , which depends on the glass thickness h_g and the incident angle of the laser beam θ_{in} , as seen in **Eq. 3b**.

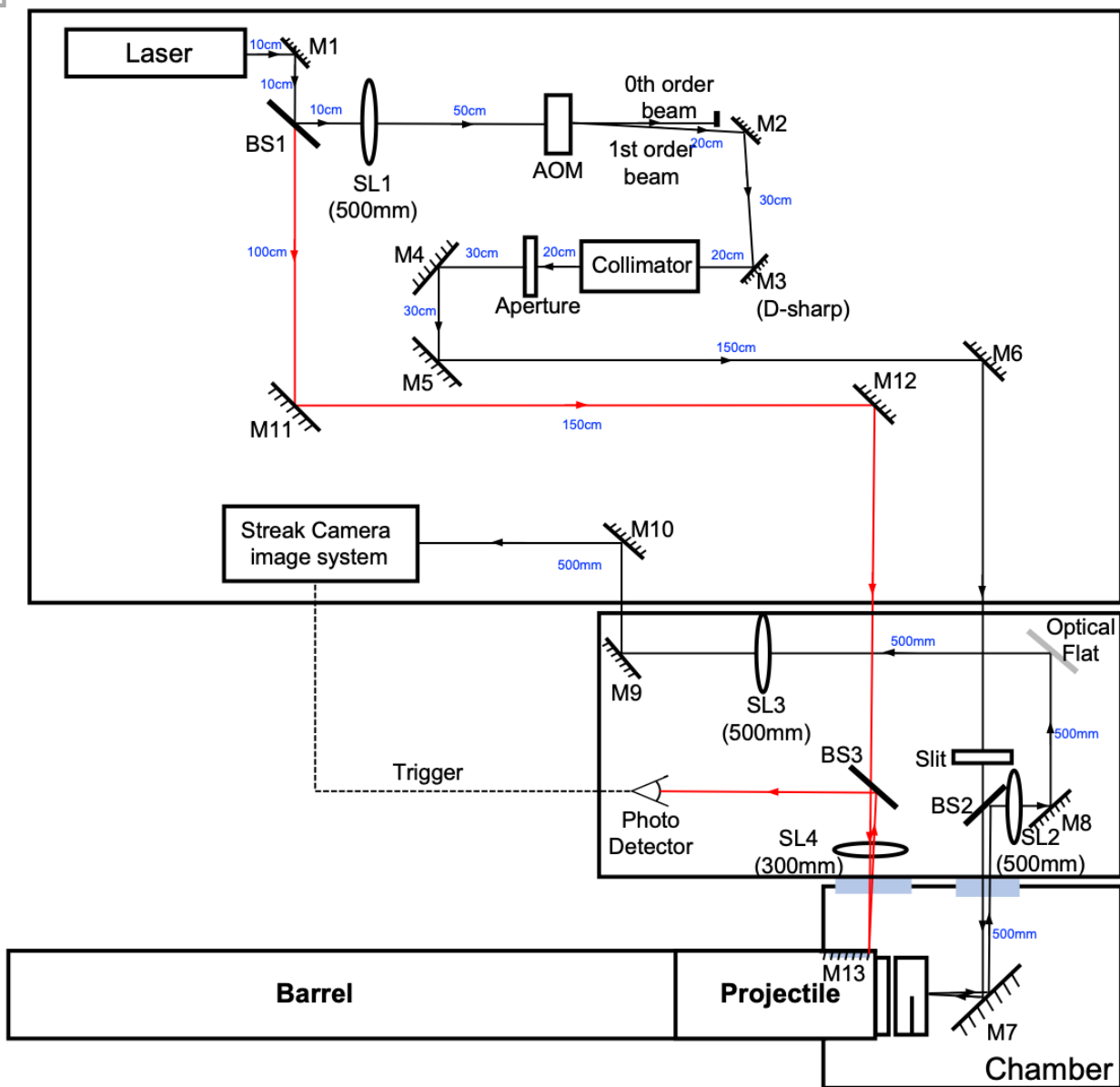


Figure 2 Optical schematics of dynamic line-image shearing interferometer (DL-ISI) in the plate impact experiment. The black solid line represents the DL-ISI optical circuits, the red solid line represents the optical triggering circuits for the streak camera system. SL represents the spherical Lens; M represents the mirror.

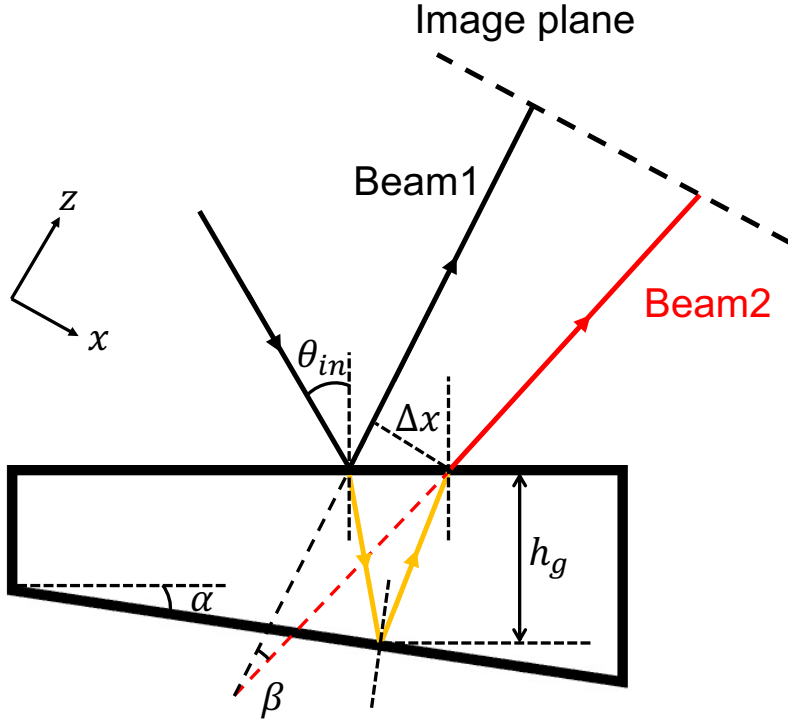


Figure 3 Schematics of two beams reflected from the front surface and rear surface of a glass plate with thickness h_g and a small tilt angle α .

3 A deep-learning framework to inversely determine cohesive parameters from *dynamic big-data-generating experiments*

In this section, we present a deep-learning framework that can inversely determine the accurate cohesive parameters in dynamic *big-data-generating experiments*. The general deep learning framework is illustrated in **Fig. 4**. The key components of the framework include: (I) a novel experimental technique to collect sufficient experimental data in a single experiment such as the DL-ISI measurement; (II) a computational simulation method to obtain a training dataset within a reasonable time span; (III) a deep-learning algorithm that has the capability to train the network and validate the prediction.

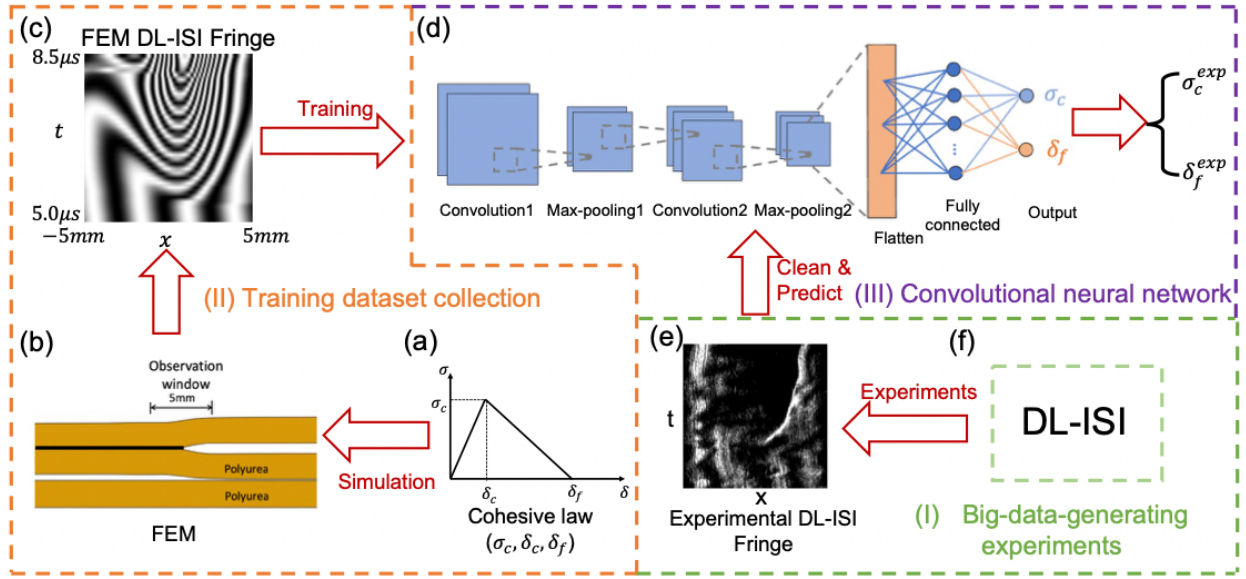


Figure 4 A deep learning framework to inversely determine cohesive parameters from dynamic *big-data-generating experiments*. (a) A linear traction-separation cohesive laws with three parameters (σ_c , δ_c , and δ_f). (b) Finite element simulations with the interfacial cohesive laws. (c) The Dynamic Line-Image Shearing interferometry (DL-ISI) fringes are generated from FEM. The horizontal axis represents spatial information, while the vertical axis represents temporal information. (d) A convolutional neural network (CNN) is composed of two convolutional layers, two max-pooling layers, one flattened layer, and one hidden layer for two outputs (σ_c , δ_f). (e) The experimental DL-ISI fringes were generated from the streak camera system. (f) Dynamic plate impact experiments with DL-ISI setups.

3.1 Dataset preparation from FEM simulations

Training a deep-learning neural network usually requires an adequate training dataset. In our case, the input variables would be a DL-ISI fringe image, and the output variables would be three cohesive parameters (σ_c , δ_c , δ_f) of a bilinear interfacial cohesive law (Fig. 4(a)). Since the dynamic crack initiation and growth primarily depends on the fracture toughness of the interface, $G = \frac{1}{2} \sigma_c \delta_f$, we consider the two cohesive parameters (σ_c , δ_f) as the output variables and set $\delta_c =$

$$G = \frac{1}{2} \sigma_c \delta_f$$

$0.2\delta_f$ for simplicity. The relevant parameter space of the output variables is selected as $\sigma_c \in [150, 350] MPa$, $\delta_f \in [0.05, 0.15] mm$, which yields the interfacial fracture toughness $G \in [3750, 26250] J/m^2$. This toughness parameter space covers the spall strength of homogeneous microcrack nucleation in the bulk material and the craze dimension estimated from postmortem fracture surfaces. Therefore, we think this parameter range is representative of the cohesive laws for polyurea. The parameter space is uniformly discretized into $m \times m$ intervals. Therefore, the total number of training samples is $M = (m + 1)^2$. We chose $m = 9, 13, 19, 24, 30$, which yields $M = 100, 196, 400, 625, 961$, to explore the effect of the training dataset on the neural network performance.

Next, we carried out FEM simulations to obtain the training dataset, i.e., the computational fringes with the labeled cohesive parameters. The FEM simulations on plate impact experiments were performed by ABAQUS/Explicit 2017 package. As shown in **Fig. 4(b)**, a flyer made by polyurea with a thickness of 2.22mm impacts a polyurea sample with a mid-plane crack. The simulations were conducted under the 2D plane-strain condition. To reduce the effects of boundary waves on the surface motion, the simulation domain was chosen as the same size as the experimental samples, i.e., the length is 50mm. The impact speed of the flyer is defined as an initial condition of 204m/s. The left half portion of the interface is considered bonded with a cohesive law. Each cohesive law with two cohesive parameters (σ_c, δ_f) was implemented as a VUINTER subroutine of the ABAQUS in the simulation. The strain energy of polyurea can be expressed as, $\bar{W}(\bar{I}_1, J) = C_{10}(\bar{I}_1 - 3) + f(J)$, where $f(J) = -A(J^{-N-1} - J^{-M-1})$ (Clifton and Jiao, 2015), where \bar{I}_1 is the invariant of the left Cauchy-Green tensor, and J is the volume ratio between the current and reference volumes. Here, $C_{10} = 150 MPa$, $A = 858 MPa$, $N = 6$, and $M = 3$, and the density of polyurea is $1070 kg/m^3$. This instantaneous finite deformation constitutive law of

polyurea represents the material characteristics well when simulating the spall experiments. Therefore, quasi-linear viscoelasticity was not considered in modeling the bulk behaviors of polyurea. Polyurea was modeled through a user subroutine VUMAT in the ABAQUS. The gradient mesh was adapted for which the smallest mesh size around the crack tip is $50\mu\text{m}$. All solutions reported here are the final convergent solutions checked by mesh sensitivity tests. The average wall time of each simulation was 10s when running on a CPU with 24 cores. The total training dataset collection for 961 simulations took ~ 3 hours. After each simulation, the displacement profile along a line within 10mm observation window size at the middle of the target's rear surface was extracted. Then, displacement gradients along the line were calculated to plot corresponding computational DL-ISI fringe images based on the theoretical derivations in **Section 2**. Each simulated DL-ISI fringe image was then cropped into a time window of interest, i.e., the initial crack-tip opening/running/arrest period and rescaled into 64×64 pixels for training. An example of a cropped computational fringe image is shown in **Fig. 4(c)**.

To explore the fringe sensitivity to the detailed cohesive laws, the DL-ISI fringes from 3 different cohesive laws: bilinear, trapezoid, and exponential laws, with the same fracture toughness, were plotted in **Fig. A.1** in **Appendix A**. As we can see, the fringe images are similar, and the image correlations among them are larger than 0.98. Therefore, our DL-ISI fringes are mainly governed by fracture energy, and it has less sensitivity to the detailed cohesive laws. However, the wall time for each FEM simulation with the exponential cohesive law is almost twice longer than the bilinear cohesive law. Hence, in this paper, we will use the bilinear traction-separation cohesive law for computational efficiency.

3.2 Convolutional neural network (CNN)

The recent development of convolutional neural network (CNN) has shown a solid capability to classify images into thousands of labels (Krizhevsky et al., 2012), which has an enormous impact on modern technology such as face recognition (Parkhi et al., 2015) and self-driving cars (Bojarski et al., 2016). Here, we adopted a CNN-based neural network to train our computational fringe images with labeled cohesive parameters. The fringe images were first fed into a convolution layer with the rectified linear activation function (ReLU), followed by a conventional 2×2 max-pooling layer. Then, the output was flattened and fed into a fully connected layer for two outputs σ_c , and δ_f , respectively. To validate and test the CNN network, the total dataset was randomly divided into 80% training dataset, 10% validation dataset, and 10% test dataset. The accuracy metrics in estimating cohesive parameters were represented by the Mean Absolute Percentage Error (MAPE) as,

$$MAPE = \frac{1}{N} \sum_{i=1}^N \left| \frac{y_i^{true} - y_i^{pre}}{y_i^{true}} \right| \times 100\%. \quad (8)$$

Where N is the number of the dataset, and y_i^{true}, y_i^{pre} are ground-true values and predicted values for the cohesive parameters. The CNN optimized the Mean Square Error (MSE) loss by using the Adam optimizer (Kingma and Ba, 2014) with the learning rate of 0.0001 for 2000 epochs on the open-source platform TensorFlow V2.5 (Abadi et al., 2016). The total training time for the dataset with 961 fringe images on an 8-core CPU is around 5 mins.

3.3 Train and test

To validate the training process as well as prevent unexpected training issues such as overfitting, the MAPE of training and validation datasets for σ_c and δ_f as a function of the training epoch is plotted in **Fig. 5(a)&(b)**, respectively. As we can see in **Fig. 5**, the MAPEs of both training and

validation datasets drop rapidly to 2% when the training epoch reaches ~ 250 , which validates the effectiveness of the current architecture. The MAPEs of both σ_c and δ_f gradually decrease to targeted 1% as the training epoch increases. It is worth noting that the MAPE for validation datasets is slightly higher ($\sim 0.5\%$) than the train datasets. This discrepancy exists for all dataset sizes and CNN architectures we considered. It may be due to the limitation of fringe sensitivity to cohesive parameters. Therefore, decreasing the train dataset mesh to increase the train dataset size does not help. Nevertheless, the overall performance of the current CNN architecture with MAPE less than 1% has already suppressed many exiting inverse algorithms for cohesive parameter determinations for nonlinear materials.

To observe the prediction performance on individual case, the predicted and ground-truth cohesive parameters are plotted in **Fig. 6(a)&(b)** for the training and testing datasets, respectively. The coefficients of determination (R^2) between predicted and true values were also calculated to illustrate the training and prediction performance. With the 2-block CNN architecture, the R^2 values on the training dataset are greater than 0.999 for both σ_c and δ_f . The R^2 values on the test dataset for both parameters are greater than 0.997, which illustrates that the current deep learning architecture can inversely identify the cohesive parameters from the given fringe images, and there is no overfitting on the training datasets.

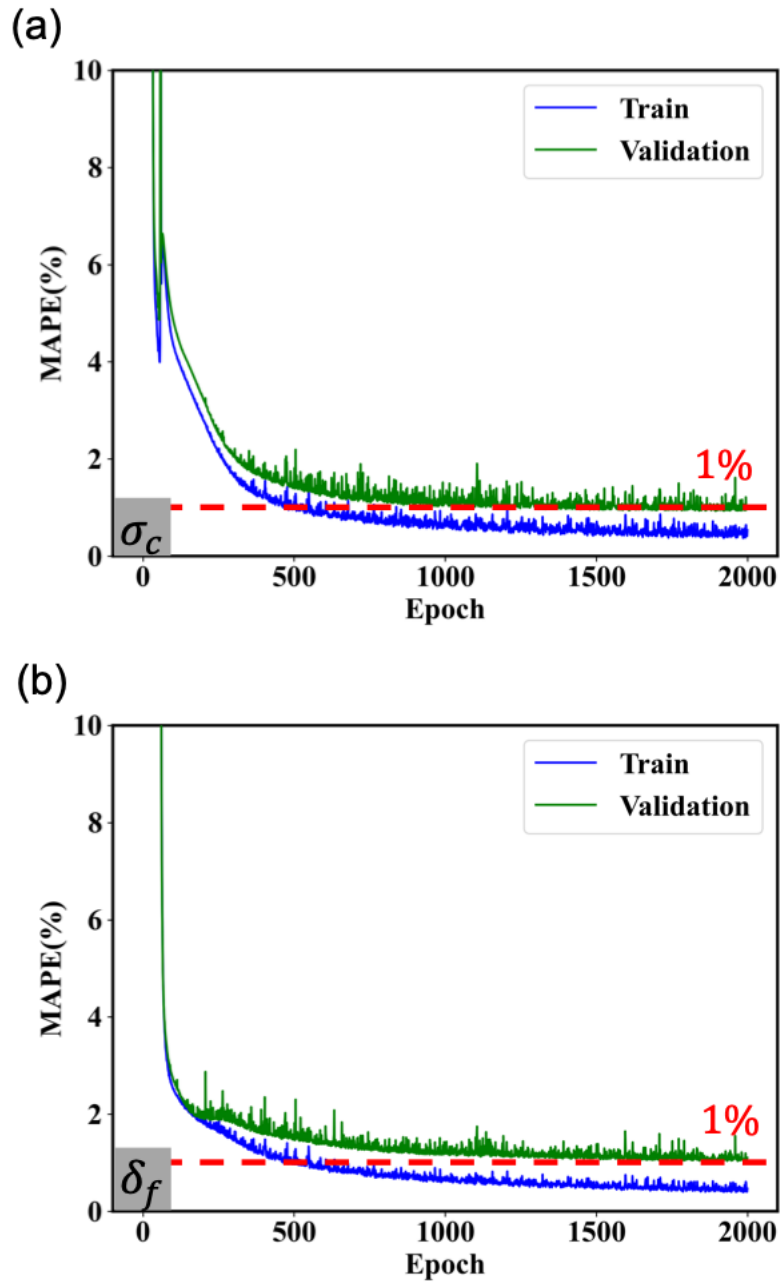


Figure 5 The Mean Absolute Percentage Error (MAPE) of training and validation datasets as a function of train epoch for (a) σ_c , and (b) δ_f with total number of 961 FEM datasets.

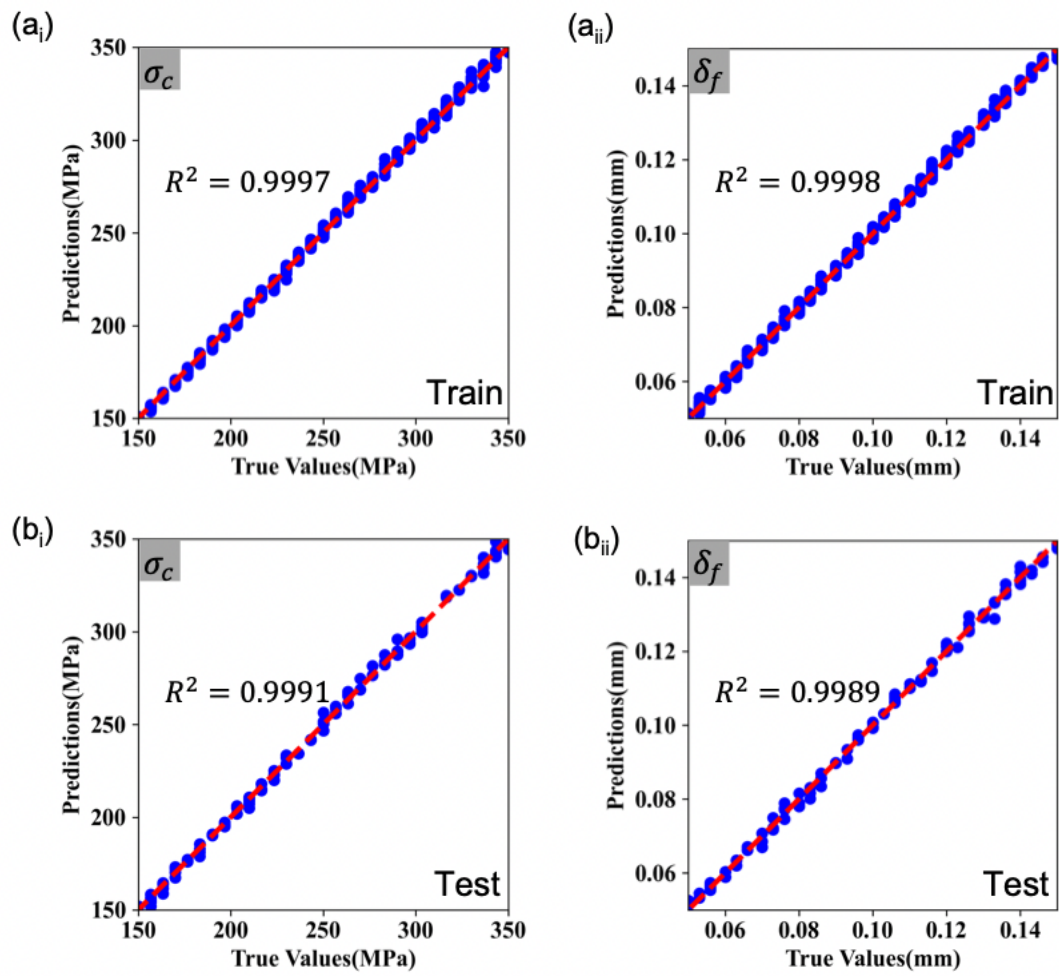


Figure 6 Prediction preformation of cohesive parameters on training datasets for (a_i) σ_c , and (a_{ii}) δ_f , and testing datasets for (b_i) σ_c , and (b_{ii}) δ_f .

4 Experiments

4.1 Design of polyurea specimen with mid-plane crack

Designing a polyurea sample with a sharp and straight mid-plane crack is crucial in the plate impact experiment. We made the sample through an innovative injection method. First, polyurea solution was prepared from the mixture of an oligomeric diamine, Versalink P-1000 (Air Product) with a diisocyanate, Isonate 143L (Dow Chemicals) in a 4:1 ratio. The P-1000 and Isonate 143L mixture was stirred by a glass stirring rod for 1 min at ambient conditions and degassed for 6 mins in a vacuum chamber. Then the degassed mixture was poured into a syringe. As shown in **Fig. 7(a)**, the syringe symmetrically injected the mixture into two sides of an acrylic mold which was coated with polyurea release spray. A Teflon thin film with a thickness of $50\mu m$ was firmly clamped in the bottom half of the acrylic frames and sandwiched between two supportive plates. As the injection proceeded, the mixture automatically lifted the supportive plates while keeping the Teflon thin-film straight. The polyurea specimen was cured and stored in a desiccator at room temperature for at least 72 hours before demolding. The demolded specimen was cut into $50mm \times 50mm$ size with mid-plane crack aligned in the middle of the sample, as shown in **Fig. 7(b)**. In this way, a polyurea specimen was prepared to have a sharp mid-plane crack and glossy surface quality for aluminum coating was prepared. The polyurea flyer was directly molded to a disk shape with a $50mm$ diameter. The flyer and the specimen were molded from the same batch of mixture solution to ensure their material properties were the same. Both flyer and specimen were coated with 200nm aluminum coating for conductivity for the tilt triggering and reflectivity for the DL-ISI measurement. The Teflon thin film was removed for the first two shots, but it was found the compressive wave will partially self-heal the mid-plane crack in the second shot. Therefore, the Teflon thin film was kept in the third shot.

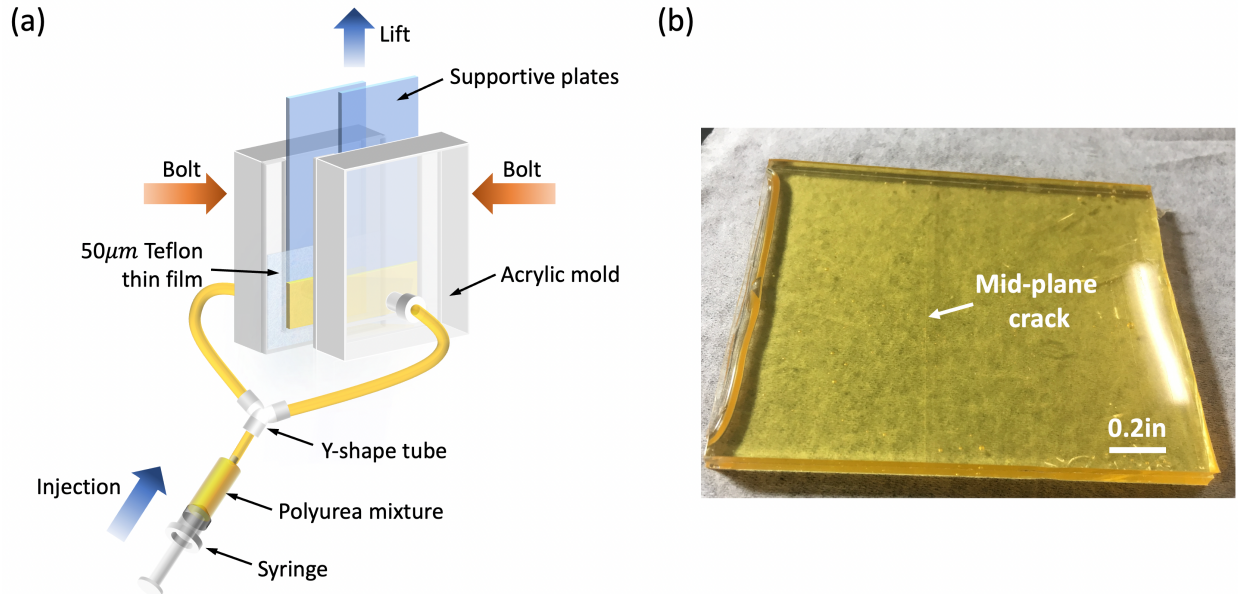


Figure 7 (a) Injection molding setup to mold polyurea with a sharp mid-plane crack. Polyurea mixture is symmetrically injected by a syringe into two sides of an acrylic mold, filling the space initially occupied by two supportive PMMA plates which sandwich and keep a $50\mu\text{m}$ -thickness Teflon film flat to create the mid-plane crack, while the plates are lifted from the mold. (b) Molded polyurea specimen with a mid-plane crack.

The thickness of the flyer and the specimen is determined based on the time-distance diagram, as shown in **Fig. 8(b)**. When the flyer impacts the specimen, compressive waves are generated. When these two waves arrive at the rear surface and reflect as tensile waves, the crack will be loaded for a duration of $t_{load} = \frac{2h}{c_l}$, where h is the thickness of the flyer, and C_l is the longitudinal wave speed of polyurea. To ensure the observation time window on the rear surface (t_{sd}, t_{ed}) is within the streak camera sweep time window, the thickness of the flyer is selected $h = 2.22\text{ mm}$, while the thickness of the sample is $H = 2h = 4.44\text{ mm}$.

4.2 Streak-camera triggering-system design

The streak camera system has an intrinsic delay time which depends on the sweeping time. If the sweeping time is set as $T_{sweep} = 20\mu s$, the time difference between triggering the streak camera sweep and the beginning of the sweeping image is $T_{delay} = 13.2\mu s$. Therefore, if we trigger the streak camera system at the impact, we will miss the observation window. Triggering the system ahead of the impact is crucial to record the fringe evolution within the window of interest. Here, we designed an optical triggering method, where the optical triggering circuit is illustrated as red lines in **Fig. 2**. After the fine alignment between the impact faces of the flyer and the specimen, an acrylic spacer with uniform thickness $d_{sp} = 3.88mm$ is placed in between, as shown in **Fig. 8(a)**. Then, a mirror with a sharp edge is mounted inside the fiberglass projectile. The optical circuit is aligned such that the beam reflected from the edge of the mirror is focused onto a photodetector, which triggers a delay generator (DG645) that controls the streak camera system. The rise time of the photodetector is 100ns, which is negligible in our case. The triggering sequence is illustrated in **Fig. 8(c)**. The time when the streak camera gate is triggered by the photodetector is denoted as T_0 . Then the streak camera sweep is triggered at $T_1 = 2\mu s$. The sweeping image starts at $T_2 = T_1 + T_{delay} = 15.2\mu s$, and ends at $T_4 = T_2 + T_{sweep} = 35.2\mu s$. Suppose the impact speed of the projectile is $V_0 = 210m/s$, the time at impact will be $T_3 = \frac{d_{sp}}{V_0} = 18.48\mu s$. In this triggering sequence design, the $10\mu s$ window of interests after impact will be centered within the $20\mu s$ sweep time. This triggering design can also accommodate a spacer alignment error up to $1mm$ or an impact speed error up to $\pm 50m/s$.

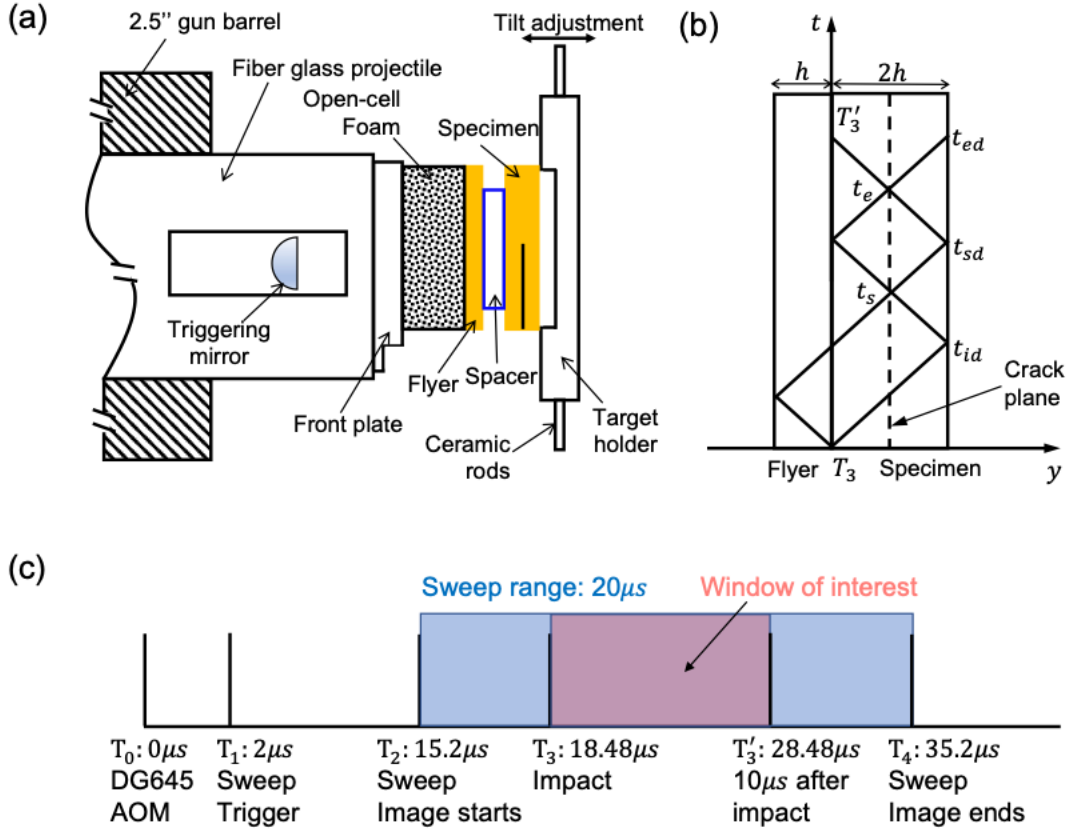


Figure 8 (a) Delay triggering setup for the streak camera system. (b) Time-distance diagram for symmetric impact on a specimen with a mid-plane crack. (c) Triggering sequence design.

4.3 Plate impact experiments

The plate impact experiments were conducted by a 2.5-inch diameter single-stage gas gun. The detailed experimental procedure for conducting plate impact experiments can be referred to previous Ph.D. theses at Brown University (Espinosa, 1992; Grunschel, 2009; Kim, 1980; Ravichandran, 1987). Here, key experimental procedures are briefly described below.

The thicknesses of the flyer and the specimen were 2.22mm and 4.44mm, respectively. To reach an ideal stress-free boundary on the rear surface of the flyer, a rigid open-cell foam with 5mm thickness was glued between the aluminum front plate of the projectile and the flyer. The aluminum front plate was mounted on a center-grounded fiberglass projectile tube. An “O” ring at

the end cup of the projectile helped prevent gas from leaking to the front. A Teflon key was used to prevent the rotation of the projectile in the gas gun barrel with a keyway. The total mass of the projectile and triggering mirror assembly was around 580g. The polyurea specimen with mid-plane crack was mounted on a Delrin sample holder, which was fixed in an adjustable base by four ceramic rods. An optical alignment technique developed by Kumar and Clifton could ensure the tilt angle between the flyer and the sample within $2 \times 10^{-5} rad$ (Kumar and Clifton, 1977). The projectile was accelerated by a sudden release of nitrogen gas. The velocity of the projectile was measured from the times at which five pairs of wire pins with known distances were shortened by the front plate. The parallelism between the flyer and the projectile was measured from the times at which four tilt pins that were glued at the corners of the specimen were shortened by the aluminum coating on the flyer. The first contact pin triggered the KEYSIGHT oscilloscope for velocity, tilt, and DG645 reference signals. The plate impact experiments were conducted in a vacuum condition to minimize the air cushion between the flyer and the specimen. A good vacuum level between 60 *mTor* and 80 *mTor* was desired. Corrugated lead plates were filled in a catcher tank to decelerate the projectile and the sample after the impact process was completed.

5 Results and discussions

We performed three shots with impact speeds of the projectile V_0 ranging from 164 m/s to 210m/s. The experimental results are summarized in **Table 1**. Among these three shots, we successfully captured the DL-ISI fringe within the desired window in the third shot. The DL-ISI parameters are listed in **Table 2**.

Table 1 Summary of experimental results. H is the thickness of the specimen with a mid-plane crack, h is the thickness of the flyer, V_0 is the impact speed of projectile, θ_t is the tilt angle, σ_0 is the normal stress, and Δc is the crack growth length.

Shots No.	h (mm)	H (mm)	Teflon	V_0 (m/s)	θ_t (mrad)	σ_0 (MPa)	Δc (μm)
HJ1901	1.98	4.44	N	164	1.70	184	400
HJ2001	2.22	4.33	N	209	2.44	234	297
HJ2101	2.25	4.38	Y	204	3.04	229	306

Table 2 DL-ISI parameters in HJ2101

Description	Notation	Value
Wavelength of laser	λ	532nm
Laser beam length	L_b	10mm
Laser beam width	W_b	2mm
Streak camera slit width	W_{sk}	100 μm
Refractive index of glass plate	n_g	1.52
Beam incident angle	θ_{in}	45 $^{\circ}$
Glass thickness	h_g	150 μm
Image plane distance	f_{img}	500mm

5.1 DL-ISI fringes

The raw experimental fringe image from the streak camera system for Shot 2101 is shown in **Fig. 9**. The horizontal axis represents the spatial information in a line perpendicular to the crack plane at the rear surface with $x = 0$ aligned at the initial mid-crack tip position, while the vertical axis represents the temporal information with $t = 0\mu s$ denoting the time at impact.

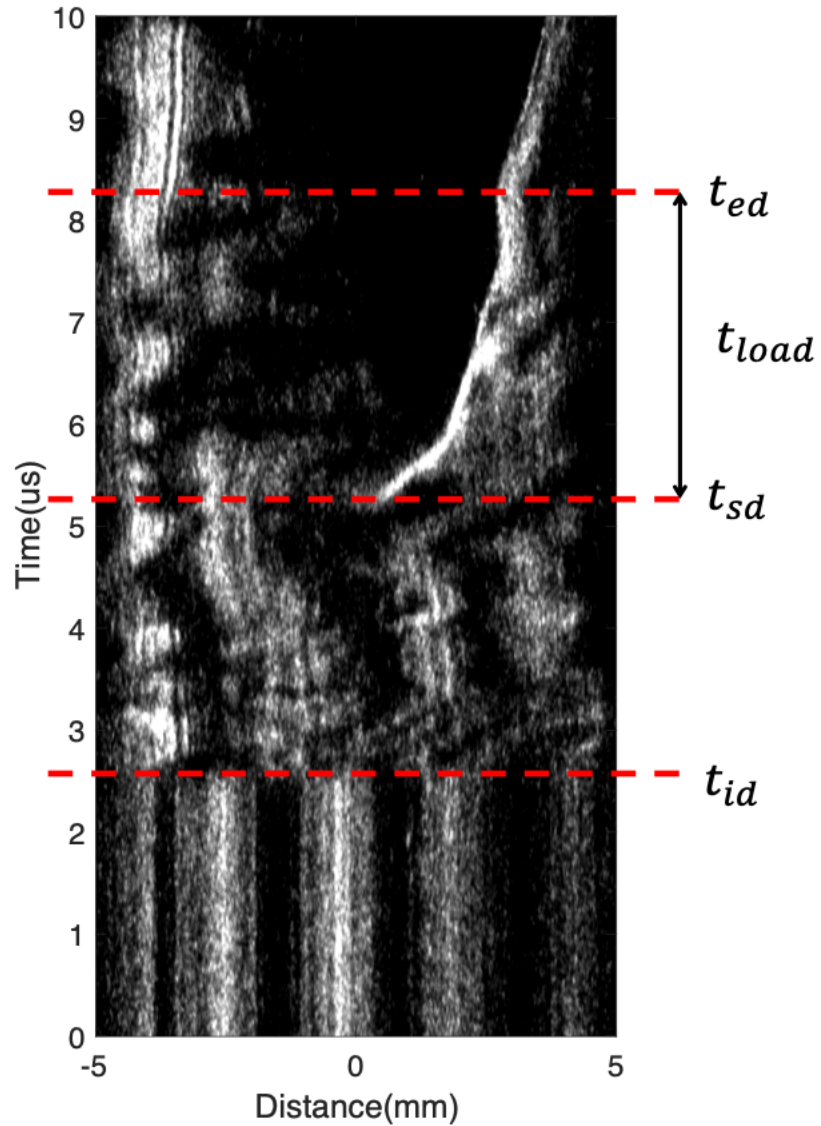


Figure 9 Raw experimental DL-ISI fringe image measured from Shot HJ2101. The time markers correspond to those in **Fig. 8(b)**.

To correct the image noise and inhomogeneous illumination issues of the streak camera system, the raw experimental fringe image was filtered by the 3×3 low pass filters and then passed through an intensity-normalization filter. The resultant fringe image is shown in **Fig. 10(a)**. To understand the general feature of the experimental fringe, a benchmark FEM simulation with a perfectly bonded interface condition is performed, and the computational fringe is plotted in **Fig.**

10(b). When $t < t_{id} = 2.7\mu s$, the compressive wave has not arrived at the rear surface. Therefore, the sweeping of the initial fringe is observed. From **Eq. 7**, the number of initial fringes is estimated to be $N_{inif} = 4.2$, which is consistent with the experimental observation. The 3.04mrad tilt angle between the flyer and the specimen generated a tilt of compressive wavefront 1.7^0 , which led to a shift of initial fringe, as observed in both experimental and FEM fringe images. During the crack loading time range ($t_{sd} < t < t_{ed}$), the tensile wave reflected from the crack tip arrived at the rear surface. Thus, the fringe density varied according to the change of displacement gradient due to crack opening.

As we can see in **Fig. 10(a)**, the experimental fringe captured the correct crack loading period. However, it only displayed fringes away from the crack tip while losing the fringe information near the crack tip. There are two reasons which could lead to this phenomenon. First, the large surface-displacement gradient near the crack tip during the tensile wave loading period would yield the reflected laser beam moving out of the collimation lens (SL2 in **Fig. 2**). Therefore, the laser beam position at x in the following relation,

$$\left| x - 2 \frac{\partial u(x, t)}{\partial x} \cdot f_{len} \right| > \frac{d_{len}}{2}, \quad (9)$$

could not be observed in the experiment. Here, $d_{len} = 50mm$ is the diameter of the collimation lens, and $f_{len} = 500mm$ is the focal length. The FEM fringe which reflected this surface-warping effect is plotted in **Fig. 10(c)**. Indeed, most of the fringe information near the crack tip is missing due to the large surface-displacement gradient. Here, we only considered the surface warping effect out of the first collimation lens. However, in the experiment, some reflected laser beams could also move out of the range of the second collimation lens (SL3 in **Fig. 2**) or other optics.

Therefore, the missing portion of the fringe will be larger in the experiment, as comparing **Fig. 10(a) &(c)**.

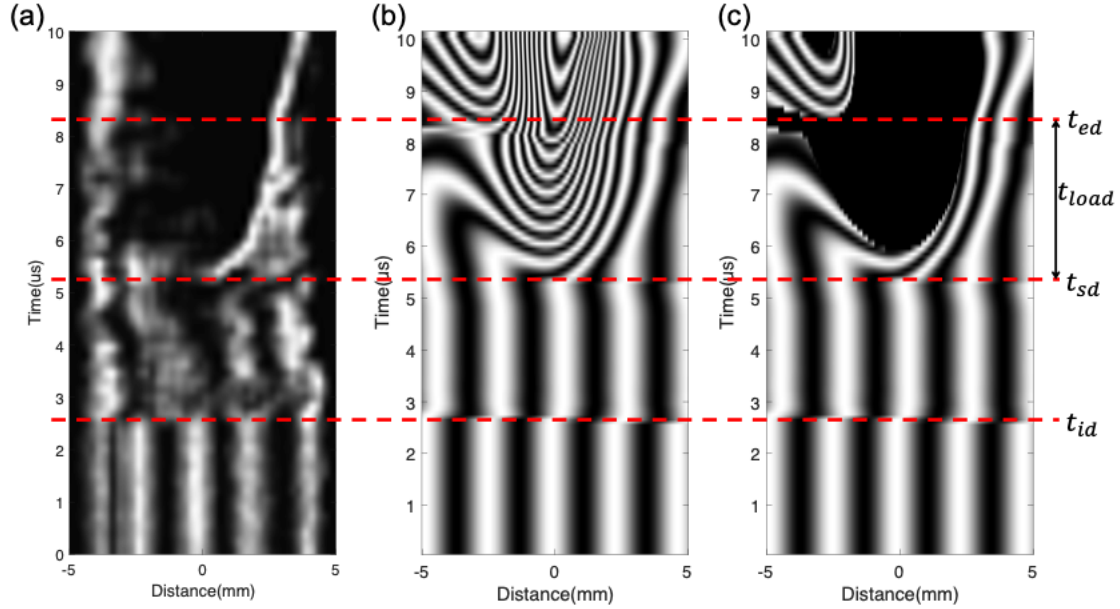


Figure 10 (a) Smoothed experimental DL-ISI fringe image; (b) Computational DL-ISI fringe image from FEM with a perfectly-bonded interface; (c) Computational DL-ISI fringe image which reflects surface-warping effect.

Second, the compressive strain at the rear surface ahead of the projected crack-tip location is found to be $\sim 6\%$ from FEM. This compressive strain is higher than the critical buckling strain of the 200nm aluminum coating on the polyurea substrate, $\varepsilon_{bc} = \frac{1}{4} \left(\frac{3E_{PU}}{E_{Al}} \right)^{2/3} \sim 4\%$, which could yield a buckling wavelength, $\lambda_{bc} = 2\pi h_{Al} \left(\frac{E_{Al}}{3E_{PU}} \right)^{\frac{1}{3}} \sim 2.3\mu m$. The buckled aluminum coating diffracted the lights to form the image with missing fringes, as observed in **Fig. 9**. Delamination or cracking of the aluminum coating could be also possible to cause the incomplete fringe image.

5.2 Physics-based DL-ISI fringe inpainting with Conditional Generative Adversarial Nets (cGAN)

As discussed in the previous section, the experimental fringe information was missing when the reflected wave from the crack-plane arrived at the rear surface of the polyurea specimen due to the large surface-displacement gradient and the failure of the aluminum coating. Nevertheless, a distinct fringe near the fringe-missing-zone boundary was successfully recorded in the experiment, whose characteristic shape is consistent with the FEM fringes. Therefore, if we could inversely obtain the missing fringes based on this boundary fringe, we could understand the crack propagation history and hence measure the dynamic fracture toughness of polyurea.

This physics-based fringe inpainting is possible because of the recent development of Conditional Generative Adversarial Nets (cGAN) (Mirza and Osindero, 2014). Although the original idea of a GAN (Goodfellow et al., 2014) is used for unsupervised learning without giving specific labels, a cGAN can generate new data based on a given condition. For example, in our case, we would like to train a cGAN model to generate a full fringe image from the given condition of a partial fringe image. Since its original development, cGAN has been successfully used in image-to-image transitions like image semantic segmentation (Rezaei et al., 2017) and image inpainting (Isola et al., 2016). As for its application in Solid Mechanics, cGAN can inversely identify the material modulus distribution from the given strain distribution images (Ni and Gao, 2021) or predict strain and stress distributions for complex composites (Yang et al., 2021a; Yang et al., 2021b). However, most current applications of cGAN in engineering have been limited to computational simulation datasets. Here, we will apply cGAN on the physics-based experimental fringe inpainting. To our knowledge, this is the first application of cGAN used for real experimental data cleaning.

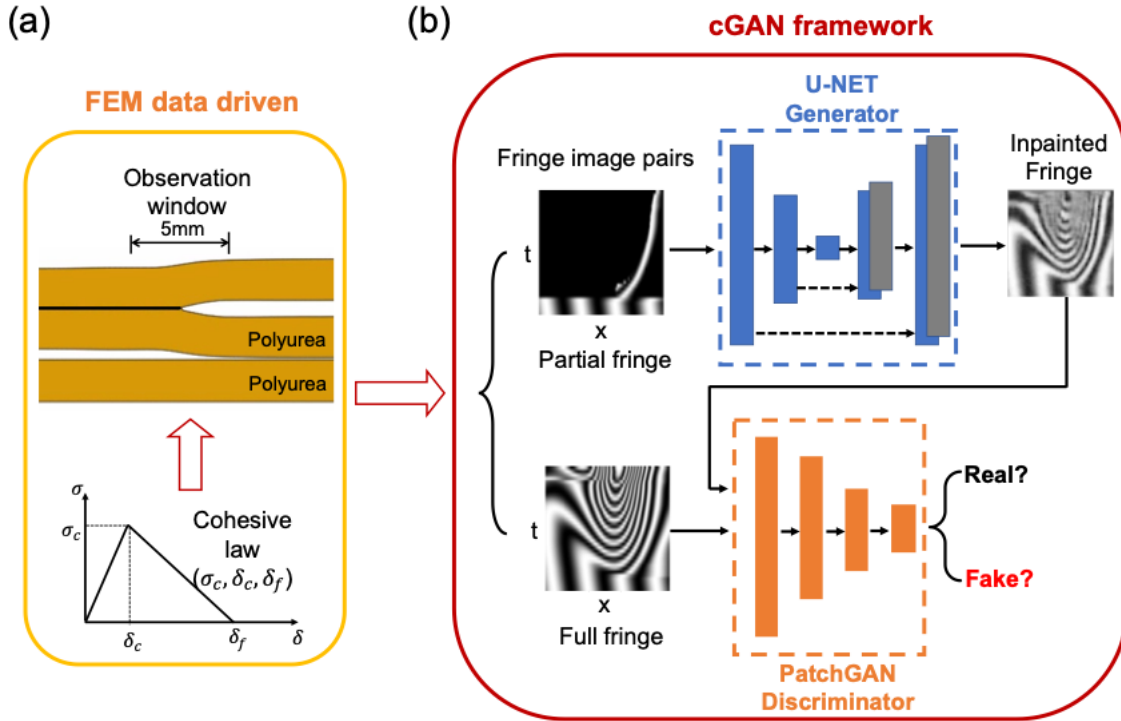


Figure 11 Schematics of the cGAN model consisted of a generator with U-NET architecture and a discriminator with PatchGAN architecture for the physics-based DL-ISI fringe inpainting.

As shown in **Fig. 11**, the typical cGAN model consists of a generator with U-NET architecture (Ronneberger et al., 2015) and a discriminator with PatchGAN architecture (Isola et al., 2016). The U-NET with skip-connection techniques is used to generate the full fringe images from the input of the given missing fringe images, while the PatchGAN evaluates the generated fringe images by comparing with the input images patch by patch. During training, the generator generates new fringe images as authentic as the ground-true fringe images while the discriminator learns to perform better to distinguish the new image from the ground truth. The performance of these two adversarial networks improves until reaching a Nash equilibrium when the generated fringe image is too real to be distinguished by the discriminator.

The cGAN model was trained on a dataset with 961 pairs of full and partial fringe images obtained from FEM with different 2-parameter (σ_c, δ_f) bilinear cohesive laws. To produce a training dataset as consistent as the experimental fringe, the displacement gradient at the rear surface that satisfies **Eq. 9** was removed to produce the partial fringe images as input images. Furthermore, the left portion of the computational fringe images was removed since the aluminum coating on the left side of the rear surface was damaged. Examples of input and ground-true fringe images are shown in **Fig. 11(b)**. The total dataset with 961 fringe images was randomly split into 90% train dataset and 10% test dataset. The training fringe images were rescaled to 128×128 pixels. The normalized L2 error is used as the cGAN model performance matrices as,

$$E_{L2} = \sqrt{\frac{\sum_{i,j} (I_{ij}^{pre} - I_{ij}^{true})^2}{\sum_{i,j} (I_{ij}^{true})^2}} \times 100\%, \quad (10)$$

where I_{ij}^{true} and I_{ij}^{pre} are the intensity at pixel i, j . The detailed model architectures for generator and discriminator are listed in **Table B.1** and **B.2** in **Appendix B**. The training was performed on the open-source platform TensorFlow V2.5 (Abadi et al., 2016). The Adam optimizer (Kingma and Ba, 2014) with a learning rate of 0.0002 was used to optimize the cGAN model. The batch size was set as 32 in our model.

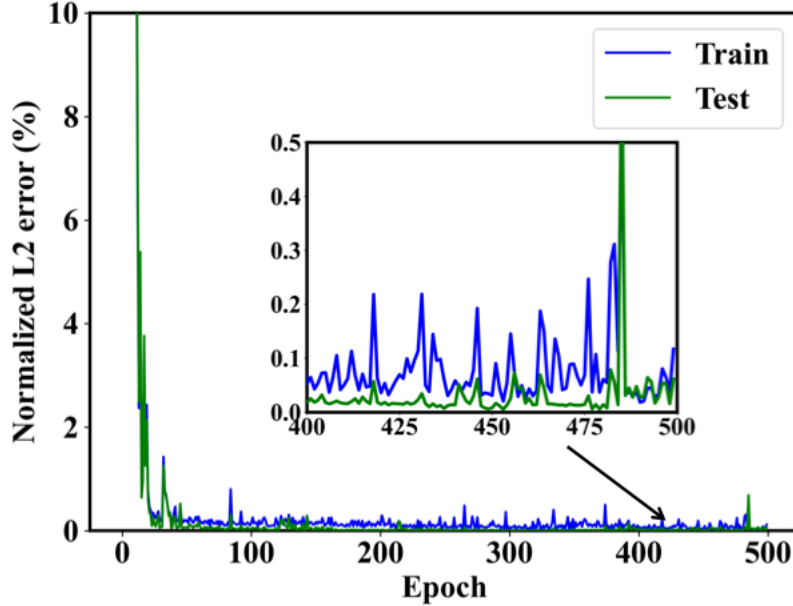


Figure 12 Training performance of the cGAN model as a function of train epoch.

The normalized L2 errors of train and test datasets as a function of train epochs are shown in **Fig. 12**. The total training time for 500 epochs on a 32-core CPU is around 8 hours. As we can see, both errors rapidly reduced to 2% after 10 epochs and converged to 0.05% after 100 epochs. The errors of train and test datasets are similar, so no overfitting is observed. Because of the image-to-image mapping capability of the cGAN model, training 200 epochs on the current cGAN model with a 961 FEM dataset is sufficient to make a prediction with a 0.05% error. To visualize the cGAN model performance, the predicted fringe images from two randomly selected input fringe images from the test datasets after 200 epochs are shown in **Fig. 13**. The pixel-wise L2 errors between prediction and ground-truth are also plotted. As we can see, the majority of pixels have an error less than 0.2%, and the pixels with the biggest errors are at the boundary of each fringe. These results illustrate the accurate performance of pixel-wise fringe inpainting from the cGAN model. Besides its high accuracy, the well-trained cGAN model is also efficient in generating a

new fringe image. For example, it takes around 5ms for the cGAN model to generate a new fringe image on a new input fringe image on a personal computer.

Cohesive Parameters	Input	Ground truth	Prediction	L2 Error (%)
$\sigma_c = 243MPa$ $\delta_f = 0.110mm$				
$\sigma_c = 183MPa$ $\delta_f = 0.106mm$				

Figure 13 Input fringe images, ground-truth fringe images, predicted fringe images, and the normalized L2 errors of two randomly selected input images in the test dataset after 200 epochs of training.

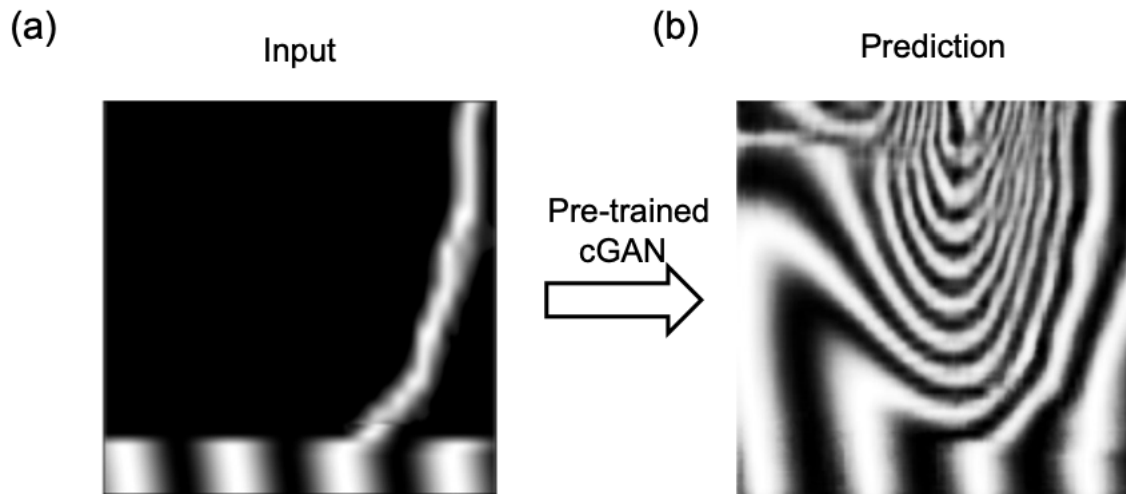


Figure 14 Fringe inpainting of experimental fringe image with initial fringe padding from pre-trained cGAN with 200 epochs.

After training the cGAN model on the FEM fringe dataset for 200 epochs, the filtered experimental DL-ISI fringe image (**Fig. 10(a)**) was cropped with a maximum correlation window with FEM datasets and rescaled to 128×128 pixels as the input image to generate the inpainted fringe image. Compared with the FEM fringe image, the experimental fringe image does not have clear initial fringes due to the surface tilt effect. To be consistent with the FEM train dataset, we prepared an experimental fringe image input with initial fringe padding from FEM as well. Then, the padded fringe image was processed with histogram equalization with the FEM inputs. The processed experimental fringe is shown in **Fig. 14(a)**. The inpainted fringe images from the input images are shown in **Fig. 14(b)**. The missing fringes were able to be inpainted inversely from the characteristic boundary fringe measured in the experiment. It is worth noting that the generated fringe image becomes locally blurred and zigzag, especially where the fringe density is high, compared with the FEM dataset. It is because the characteristic fringe is not as smooth as in the FEM dataset, which could produce noise when the cGAN model makes the prediction. Nevertheless, the pre-trained cGAN model with a computational dataset is capable of generating a physics-based full-field fringe image from the experimental data.

5.3 Cohesive parameters and dynamic fracture toughness of polyurea

Since we obtained the full-field fringe image during the crack loading process from the cGAN model, the cohesive parameters could be ideally determined through the deep learning framework proposed in **Section 2**. However, as discussed in the previous subsection, the inpainted fringe is locally zigzag and noisier compared with the FEM dataset, reducing the accuracy of CNN predictions. Here, we calculate the correlations between the inpainted fringe and each FEM fringe in the FEM dataset, and statistically determine the cohesive parameters as well as the fracture

toughness. The CNN prediction is also then included for comparison. The correlation coefficient is defined as,

$$cor = \frac{\sum_{i,j} (I_{ij}^{exp} - \bar{I}^{exp})(I_{ij}^{FEM} - \bar{I}^{FEM})}{\sqrt{\sum_{i,j} (I_{ij}^{exp} - \bar{I}^{exp})^2 \sum_{i,j} (I_{ij}^{FEM} - \bar{I}^{FEM})^2}}, \quad (11)$$

where I_{ij}^{exp} and I_{ij}^{FEM} are the intensity at pixel i,j for experimental and FEM fringe image, respectively. \bar{I}^{exp} and \bar{I}^{FEM} are the mean values. The correlation coefficients are plotted in **Fig. 15**. The correlation coefficients are in the range of 0.35~0.89. To determine the cohesive parameters as well as the standard deviations, the correlation coefficients with $cor > 0.75$ are fitted into a bivariate normal distribution. The prediction results are summarized in **Table 3**. The predicted cohesive parameters with error bars are marked in yellow in **Fig. 15**. The dynamic fracture toughness of polyurea under an extremely high rate of crack-tip loading $\dot{K} \sim 10^7 \text{ MPa}\sqrt{\text{m}}/\text{s}$ is determined as $G_c = 12100 \text{ MPa}$ with a standard deviation of 1100 MPa . The estimation of dynamic fracture toughness based on the linear elastic fracture mechanics (LEFM) theory is $G_c^{LEFM} = 13418.62 \text{ J/m}^2$ (Details in **Appendix C**), which overestimates $\sim 11\%$. The CNN prediction based on 7 independent trainings is summarized in **Table 3** and marked in green in **Fig. 15**.

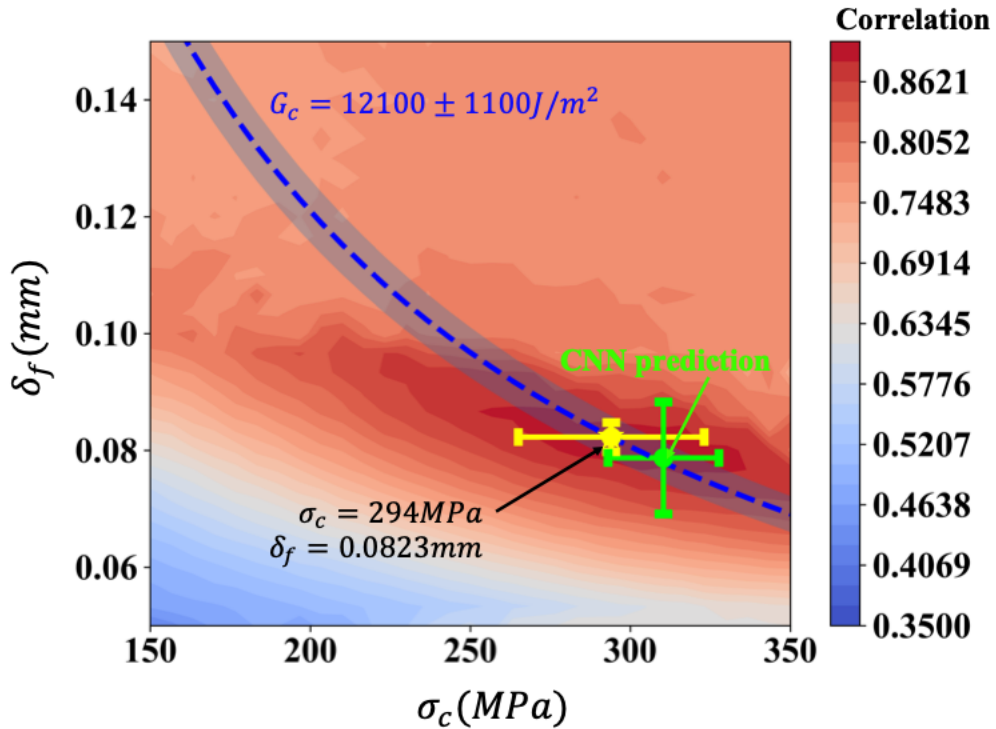


Figure 15 Correlation coefficients contour between the experimental fringe and 961 FEM fringes in the dataset. The cohesive parameters with error bars determined from bivariate normal distribution are marked in yellow. The dynamic fracture toughness is marked in blue dotted line with shaded error bar. The CNN predictions with error bars are marked in green.

Table 3 Cohesive parameters predictions from the correlation and CNN methods

Correlation			CNN		
$\sigma_c(Mpa)$	$\delta_f(mm)$	$G_c(J/m^2)$	$\sigma_c(MPa)$	$\delta_f(mm)$	$G_c(J/m^2)$
294	0.0823	12100	$310 \pm$	0.0787	12200
± 29	± 0.0025	± 1100	17	± 0.0096	± 1700

As we can see, the CNN makes a reasonable prediction of the fracture toughness with only a 1% difference with the correlation method. However, more significant prediction discrepancies have been made in the individual parameters. Furthermore, CNN has a more significant prediction variance than the correlation methods. It is due to the difference in fidelity between our train dataset and experimental test dataset, such that our training dataset is the 2D FEM dataset with low fidelity. However, the experimental inputs have high fidelity. Therefore, constructing the correlation between these two datasets plays a crucial role in the multi-fidelity modeling method (Fernández-Godino et al., 2016). To this end, Meng and Karniadakis developed a multi-fidelity deep neural network (MFNN) that can efficiently train the datasets with different levels of fidelity (Meng and Karniadakis, 2020). For example, compared with the single-fidelity training, MFNN is capable of increasing the prediction accuracy on the material properties in the instrumented indentation when trained on a multi-fidelity dataset with both FEM and experiments (Lu et al., 2020). Therefore, as more experimental fringes are collected in future experiments, we could use MFNN to train the FEM fringes as well as the previous experimental fringes together to increase the accuracy of the predictions in the predictions of the cohesive parameters. Except for the error source from the multi-fidelity, other error sources on the predictions could come from the sensitivity of the DL-ISI fringe, cGAN, and CNN models. These errors may not be independent; thus, distinguishing the errors among these different sources is not feasible.

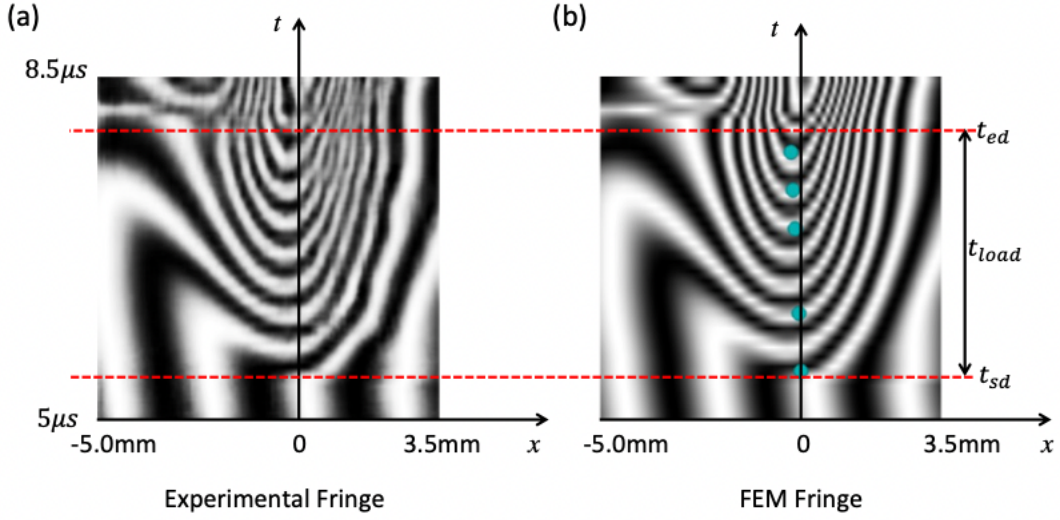


Figure 16 (a) Inpainted experimental fringe; (b) FEM fringe generated from FEM simulation with predicted cohesive parameters of $\sigma_c = 294MPa$ and $\delta_f = 0.0823mm$. The crack tip positions are labeled in green dots.

When the accurate cohesive parameters are determined, the crack growth history can be readily analyzed from the FEM. The FEM fringes generated from the simulation with the predicted cohesive parameters are plotted together with the experimental fringes in **Fig. 16**. Two fringe images are very similar, with a correlation coefficient of 0.881. The crack-tip positions are labeled in green markers on the FEM fringe image. The maximum crack growth length during the first crack loading period is $250\mu m$. To understand the crack growth process, we plotted the three crack advance distances, $a_{0.1}$, a_c , and a_f in **Fig. 17(b)**, when the separations between crack surfaces reach $0.1\delta_c$, δ_c , and δ_f as defined in **Fig. 1(b)** and shown in **Fig. 17(a)**. The result shows that a_c increases to $350\mu m$ while a_f increases to $250\mu m$ during the first period of crack loading. The fractography of the crack plane after the impact was obtained from optical microscopy and shown in **Fig. 17(c)**. The crack-tip positions with a_c and a_f are labeled in the fractography. We found the crack front of a_c is straight while the crack front of a_f is relatively wavy with the average

wavelength of $100\text{--}200\ \mu\text{m}$ and the average crack advance distance of $200\text{--}250\ \mu\text{m}$. These crack growth distances are consistent with FEM results during the first loading period. A wavy crack front with micron-scale wavelength could be caused by the local material inhomogeneity. Clusters with the size of hundred nanometers were observed in bulk polyurea from our high-resolution AFM tapping-mode morphology images. However, in the micron-scale, the polyurea sample is considered as homogenous, and linear-elastic crack-front growth instability is not expected (Gao and Rice, 1989; Rice et al., 1994). Therefore, in the experiment, the crack front when the surface separation reached δ_c is straight even though the initial stationary crack front is slightly wavy. However, the a_f crack front could be wavy as the crack-face traction softens for $\delta_c < \delta < \delta_f$. In addition, during the unloading process, the fracture wake zone can be partially healed due to the self-healing capability of polyurea, leaving local craze zone residuals on the crack plane. These residuals could enhance the apparent waviness of the post-mortem a_f crack front. Nevertheless, the 3D crack advance and self-healing processes were not considered in our FEM simulations for computational efficiency. The cohesive strength σ_c and the toughness of polyurea G_c under the crack loading rate are displayed on an Ashby diagram (Ashby, 2012) in **Fig. 18**. Under the dynamic loading, the cohesive strength of polyurea is found in the cohesive-property range of composites, which is far beyond the strength of any other polymers and rubbers.

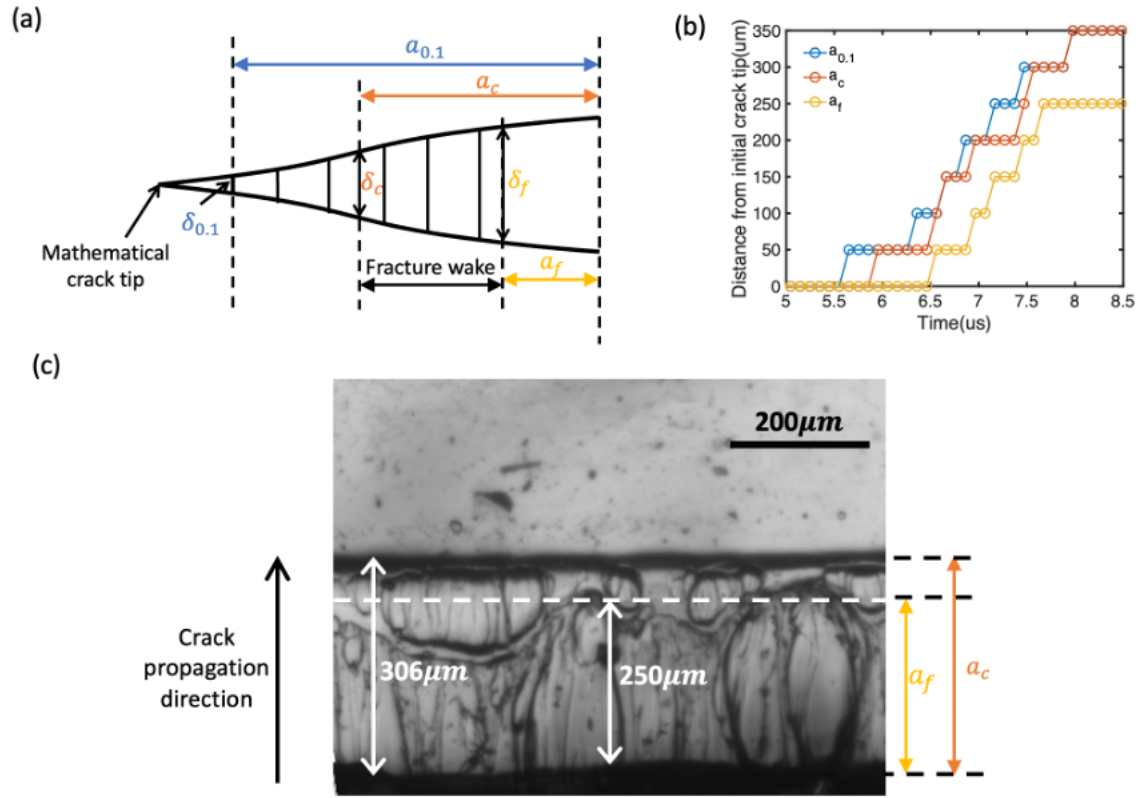


Figure 17 (a) The schematics of crack process zone. (b) The crack advance distances of $a_{0.1}$, a_c , and a_f as a function of time in the FEM simulations. (c) Fractography for Shots HJ2101.

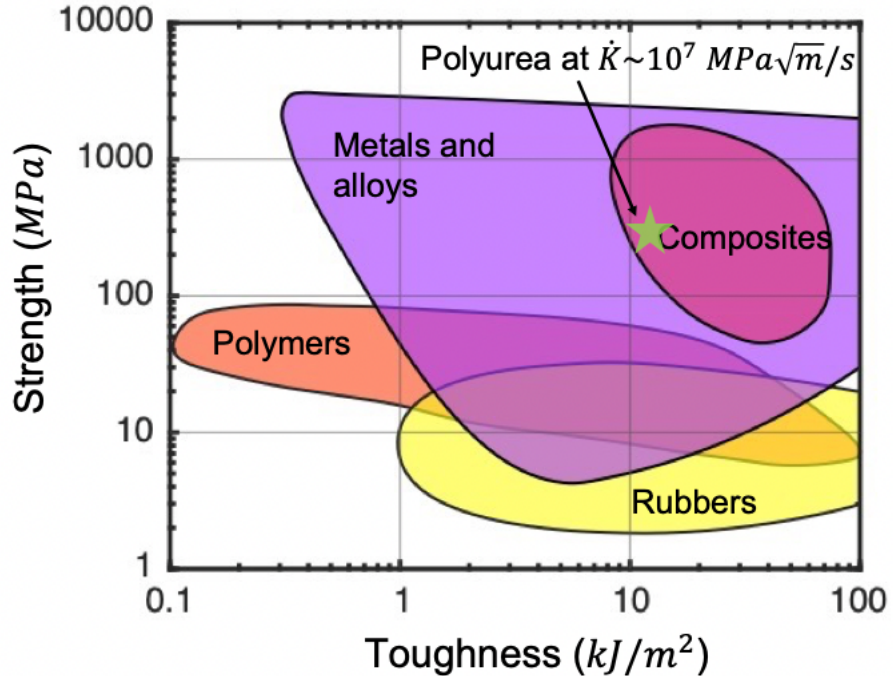


Figure 18 High dynamic fracture toughness of polyurea at a high crack-tip loading rate plotted on an Ashby diagram (Ashby, 2012).

6 Conclusion

In this paper, the dynamic toughness of polyurea PU1000 was successfully measured from a *big-data-generating experiment* with our newly invented DL-ISI, applying plane-wave loading of a mid-cracked specimen with plate impact. The experimental DL-ISI fringe inpainting is enabled from a state-of-the-art cGAN model pre-trained with a corresponding FEM dataset. The dynamic fracture toughness is measured as $G_c = 12100 \pm 1100 \text{ J/m}^2$ under a very high crack-tip loading rate, $\dot{K} \sim 10^7 \text{ MPa}\sqrt{\text{m}}/\text{s}$. Apparent dynamic toughening is found in polyurea where the cohesive strength, $\sigma_c = 294 \text{ MPa}$, under the crack-tip loading rate is found to be nearly three times higher than the spall strength $\sim 105 \text{ MPa}$ under the symmetric impact with the same impact speed. These

experimental results fill the gap in the current understanding of bicontinuously nanostructured copolymer's cooperative-failure strength under extreme local conditions near the crack tip. The underlying strengthening mechanisms were investigated through molecular-level *in-situ* experiments and mesoscale simulations, and reported in the sequel paper (Jin et al., 2021). We also believe the framework of this *big-data-generating experiment* could steer the future direction on experimental mechanics, which combines the innovative high-throughput experimental techniques with state-of-the-art machine learning algorithms for the next-level material design and characterization.

Acknowledgments

The authors gratefully acknowledge the supports provided by U.S. Office of Naval Research (Grant N00014-18-1-2513). Help on preliminary experiments from Dr. Tong Jiao is acknowledged. Helpful discussions with Mr. Enrui Zhang on deep learning section are acknowledged.

CRediT author statement

Hanxun Jin: Conceptualization, Methodology, Software, Data Curation, Validation, Writing - Original Draft

Rodney J. Clifton: Writing - Review&Editing, Supervision, Project administration

Kyung-Suk Kim: Conceptualization, Methodology, Writing - Review&Editing, Supervision, Project administration

Appendix A

DL-ISI fringe sensitivity on the detailed cohesive laws

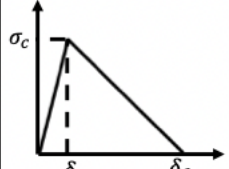
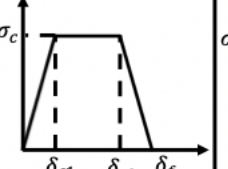
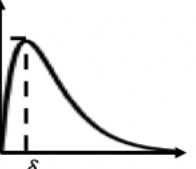
Cohesive law	Bilinear	Trapezoid	Exponential
Schematics			
Cohesive parameters	$\sigma_c = 300MPa$ $\delta_f = 0.08mm$ $\delta_c = 0.2\delta_f$	$\sigma_c = 300MPa$ $\delta_f = 0.053mm$ $\delta_{c1} = 0.25\delta_f$ $\delta_{c2} = 0.75\delta_f$	$\sigma_c = 300MPa$ $\delta_f = 0.015mm$
Fracture toughness	$G_c = 12000J/m^2$		
DL-ISI fringes			
Correlation	1.0	0.9909	0.9807
Wall time	10.8s	9.8s	18.3s

Figure A.1 DL-ISI fringe images from FEM simulations with 3 different cohesive laws: bilinear, trapezoid, and exponential laws with the same fracture energy.

Appendix B

Detailed cGAN model

Table B.1. Detailed U-Net Generator architecture.

Layer	Layer structure	Output shape
1	Input layer	(128, 128, 1)
2	Conv2D + LeakyReLU(alpha=0.2)	(64, 64, 64)
3	Conv2D + BatchNomalization + LeakyReLU(alpha=0.2)	(32, 32, 128)
4	Conv2D + BatchNomalization + LeakyReLU(alpha=0.2)	(16, 16, 256)
5	Conv2D + BatchNomalization + LeakyReLU(alpha=0.2)	(8, 8, 512)
6	Conv2D + BatchNomalization + LeakyReLU(alpha=0.2)	(4, 4, 512)
7	Conv2D + BatchNomalization + LeakyReLU(alpha=0.2)	(2, 2, 512)
8	Conv2D + BatchNomalization + LeakyReLU(alpha=0.2)	(1, 1, 512)
9	UpSampling2D + Conv2D + BatchNomalization	(2, 2, 1024)
10	UpSampling2D + Conv2D +BatchNomalization	(4, 4, 1024)
11	UpSampling2D + Conv2D +BatchNomalization	(8, 8, 1024)
12	UpSampling2D + Conv2D +BatchNomalization	(16, 16, 512)
13	UpSampling2D + Conv2D +BatchNomalization	(32, 32, 256)
14	UpSampling2D + Conv2D +BatchNomalization	(64, 64, 128)
15	Output layer	(128, 128, 1)

Table B.2. Detailed PatchGAN Discriminator architecture.

Layer	Layer structure	Output shape
1	Concatenate layer	(128, 128, 2)
2	Conv2D + LeakyReLU (alpha=0.2)	(64, 64, 64)
3	Conv2D + BatchNomalization + LeakyReLU (alpha=0.2)	(32, 32, 128)
4	Conv2D + BatchNomalization + LeakyReLU (alpha=0.2)	(16, 16, 256)
5	Conv2D + BatchNomalization + LeakyReLU (alpha=0.2)	(8, 8, 512)
6	Conv2D	(8, 8, 1)

*Layer structure uses the abbreviate terminology in TensorFlow 2.5.

Appendix C

Linear elastic fracture mechanics (LEFM) estimation of dynamic fracture toughness

From the linear elastic fracture mechanics (LEFM) theory, the Mode I crack-tip stress intensity factor as a function of time under a step loading of normal tensile wave can be expressed as (Freund, 1998),

$$K_I(t) = n(\nu)\sigma_0 C_l^{1/2} t^{1/2} \quad (C.1)$$

where $n(\nu) = \frac{2}{1-\nu} \left(\frac{1-2\nu}{\pi} \right)^{\frac{1}{2}}$ with Poisson's ratio $\nu = 0.4$ is the blunt factor, $\sigma_0 = \frac{1}{2} \rho C_l V_0$ is the incident normal stress with density $\rho = 1070 \text{ kg/m}^3$ and impact velocity $V_0 = 204 \text{ m/s}$. $C_l = \left(\frac{E_G}{\rho(1-\nu^2)} \right)^{1/2} = 2100 \text{ m/s}$ is the longitudinal wave speed. At a critical time τ , the crack is assumed to initiate, the critical Mode I stress intensity factor K_{IC} can be expressed as,

$$K_{IC} = n(\nu)\sigma_0 C_l^{1/2} \tau^{1/2} \quad (C.2)$$

Therefore, the toughness G_c under plane-strain condition is expressed as,

$$G_c = \frac{(1-\nu^2)K_{IC}^2}{E_G} \quad (C.3)$$

where $E_G = 3.96 \text{ GPa}$ is Young's modulus of the polyurea. From FEM, the incubation time of crack-growth initiation is $\tau = 0.8 \mu\text{s}$. Therefore, the linear elastic fracture mechanics (LEFM) estimation of the toughness provides $G_c^{LEFM} = 13418.62 \text{ J/m}^2$.

Reference

Abadi, M., Barham, P., Chen, J., Chen, Z., Davis, A., Dean, J., Devin, M., Ghemawat, S., Irving, G., Isard, M., 2016. Tensorflow: A system for large-scale machine learning, 12th {USENIX} symposium on operating systems design and implementation ({OSDI} 16), pp. 265-283.

Ashby, M.F., 2012. Materials and the environment: eco-informed material choice. Elsevier.

Barenblatt, G.I., 1962. The mathematical theory of equilibrium cracks in Brittle Fracture. *Adv Appl Mech*, 7, 55-129.

Bazant, Z.P., 2002. Concrete fracture models: testing and practice. *Eng Fract Mech* 69, 165-205.

Bojarski, M., Del Testa, D., Dworakowski, D., Firner, B., Flepp, B., Goyal, P., Jackel, L.D., Monfort, M., Muller, U., Zhang, J., 2016. End to end learning for self-driving cars. arXiv preprint arXiv:1604.07316.

Clifton, R., Jiao, T., 2015. Testing, Experiments and Properties of HSREP: Pressure and Strain-Rate Sensitivity of an Elastomer:(1) Pressure-Shear Plate Impact Experiments;(2) Constitutive Modeling. R.G. Barsoum (Ed.), *Elastomeric Polymers with High Rate Sensitivity: Applications in Blast, Shockwave, and Penetration Mechanics*, Elsevier Inc., pp. 17-65.

Das, S., Yilgor, I., Yilgor, E., Inci, B., Tezgel, O., Beyer, F.L., Wilkes, G.L., 2007. Structure-property relationships and melt rheology of segmented, non-chain extended polyureas: Effect of soft segment molecular weight. *Polymer* 48, 290-301.

Dugdale, D.S., 1960. Yielding of Steel Sheets Containing Slits. *J Mech Phys Solids* 8, 100-104.

Espinosa, H.D., 1992. Micromechanics of the dynamic response of ceramics and ceramic composites. Brown University, Ph.D. thesis.

Ferdousi, S., Chen, Q., Soltani, M., Zhu, J.D., Cao, P.F., Choi, W.B., Advincula, R., Jiang, Y.J., 2021. Characterize traction-separation relation and interfacial imperfections by data-driven machine learning models. *Sci Rep-Uk* 11.

Fernández-Godino, M.G., Park, C., Kim, N.-H., Haftka, R.T., 2016. Review of multi-fidelity models. *arXiv preprint arXiv:1609.07196*.

Freund, L., 1972. Crack propagation in an elastic solid subjected to general loading—I. Constant rate of extension. *J Mech Phys Solids* 20, 129-140.

Freund, L., 1973. Crack propagation in an elastic solid subjected to general loading—III. Stress wave loading. *J Mech Phys Solids* 21, 47-61.

Freund, L.B., 1998. *Dynamic fracture mechanics*. Cambridge university press.

Gao, H., Rice, J.R., 1989. A first-order perturbation analysis of crack trapping by arrays of obstacles. *J Appl Mech* 56(4), 828–836.

Goodfellow, I.J., Pouget-Abadie, J., Mirza, M., Xu, B., Warde-Farley, D., Ozair, S., Courville, A., Bengio, Y., 2014. Generative Adversarial Networks, p. *arXiv:1406.2661*.

Grujicic, M., Snipes, J.S., Galgalikar, R., Ramaswami, S., 2014. Material-Model-Based Determination of the Shock-Hugoniot Relations in Nanosegregated Polyurea. *J Mater Eng Perform* 23, 357-371.

Grujicic, M., Yavari, R., Snipes, J.S., Ramaswami, S., Jiao, T., Clifton, R.J., 2015. Experimental and Computational Study of the Shearing Resistance of Polyurea at High Pressures and High Strain Rates. *J Mater Eng Perform* 24, 778-798.

Grunschel, S.E., 2009. Pressure-Shear Plate Impact Experiments on High-Purity Aluminum at Temperatures Approaching Melt. Brown University, Ph.D. thesis.

Hong, S., Chew, H.B., Kim, K.-S., 2009. Cohesive-zone laws for void growth - I. Experimental field projection of crack-tip crazing in glassy polymers. *J Mech Phys Solids* 57, 1357-1373.

Hong, S.S., Kim, K.-S., 2003. Extraction of cohesive-zone laws from elastic far-fields of a cohesive crack tip: a field projection method. *J Mech Phys Solids* 51, 1267-1286.

Hsu, Y.C., Yu, C.H., Buehler, M.J., 2020. Using Deep Learning to Predict Fracture Patterns in Crystalline Solids. *Matter* 3, 197-211.

Isola, P., Zhu, J.-Y., Zhou, T., Efros, A.A., 2016. Image-to-Image Translation with Conditional Adversarial Networks, p. arXiv:1611.07004.

Jain, A., Youssef, G., Gupta, V., 2013. Dynamic tensile strength of polyurea-bonded steel/E-glass composite joints. *J Adhes Sci Technol* 27, 403-412.

Jin, H., Machnicki, C., Kim, K.-S. 2021. Nanophase fragmentation and self-healing of a block copolymer under deformation: in-situ AFM experiments and mesoscale simulations, in preparation.

Kim, K.-S., Jin, H., Jiao, T., Clifton, R.J., 2020. Dynamic Fracture-Toughness Testing of a Hierarchically Nano-Structured Solid, in: Xia S., Beese A., R.B., B. (Eds.), Society for Experimental Mechanics Series, Fracture, Fatigue, Failure and Damage Evolution. Springer.

Kim, K.-S., 1980. Plane wave experiments in dynamic plasticity. Brown University, Ph.D. thesis.

Kim, K.-S., Clifton, R.J., Kumar, P., 1977. A combined normal-and transverse-displacement interferometer with an application to impact of y-cut quartz. *J Appl Phys* 48, 4132-4139.

Kim, K.-S., McMeeking, R.M., Johnson, K.L., 1998. Adhesion, slip, cohesive zones and energy fluxes for elastic spheres in contact. *J Mech Phys Solids* 46, 243-266.

Kingma, D.P., Ba, J., 2014. Adam: A Method for Stochastic Optimization, p. arXiv:1412.6980.

Krizhevsky, A., Sutskever, I., Hinton, G.E., 2012. ImageNet classification with deep convolutional neural networks, Proceedings of the 25th International Conference on Neural Information Processing Systems - Volume 1. Curran Associates Inc., Lake Tahoe, Nevada, pp. 1097–1105.

Kumar, P., Clifton, R.J., 1977. Optical Alignment of Impact Faces for Plate Impact Experiments. *J Appl Phys* 48, 1366-1367.

LeCun, Y., Bengio, Y., Hinton, G., 2015. Deep learning. *Nature* 521, 436-444.

Li, Q.Y., Kim, K.-S., 2008. Micromechanics of friction: effects of nanometre-scale roughness. *P Roy Soc a-Math Phy* 464, 1319-1343.

Li, Q.Y., Kim, K.-S., 2009. Micromechanics of Rough Surface Adhesion: A Homogenized Projection Method. *Acta Mech Solida Sin* 22, 377-390.

Lu, L., Dao, M., Kumar, P., Ramamurty, U., Karniadakis, G.E., Suresh, S., 2020. Extraction of mechanical properties of materials through deep learning from instrumented indentation. *P Natl Acad Sci USA* 117, 7052-7062.

Meng, X., Karniadakis, G.E., 2020. A composite neural network that learns from multi-fidelity data: Application to function approximation and inverse PDE problems. *J Comput Phys* 401, 109020.

Mirza, M., Osindero, S., 2014. Conditional Generative Adversarial Nets, p. arXiv:1411.1784.

Mohammed, I., Liechti, K.M., 2000. Cohesive zone modeling of crack nucleation at bimaterial corners. *J Mech Phys Solids* 48, 735-764.

Ni, B., Gao, H.J., 2021. A deep learning approach to the inverse problem of modulus identification in elasticity. *Mrs Bull* 46, 19-25.

Parkhi, O.M., Vedaldi, A., Zisserman, A., 2015. Deep face recognition. Proceedings of the British Machine Vision, Vol. 1, No. 3.

Ravichandran, G., 1987. Dynamic fracture under plane wave loading. Brown University, Ph.D. thesis.

Ravichandran, G., Clifton, R.J., 1989. Dynamic Fracture under Plane-Wave Loading. *Int J Fracture* 40, 157-201.

Rezaei, M., Harmuth, K., Gierke, W., Kellermeier, T., Fischer, M., Yang, H., Meinel, C., 2017. Conditional Adversarial Network for Semantic Segmentation of Brain Tumor, p. arXiv:1708.05227.

Rice, J.R., Ben-Zion, Y., Kim, K.-S., 1994. Three-dimensional perturbation solution for a dynamic planar crack moving unsteadily in a model elastic solid. *J Mech Phys Solids* 42, 813-843.

Ronneberger, O., Fischer, P., Brox, T., 2015. U-Net: Convolutional Networks for Biomedical Image Segmentation, p. arXiv:1505.04597.

Sanchez-Lengeling, B., Aspuru-Guzik, A., 2018. Inverse molecular design using machine learning: Generative models for matter engineering. *Science* 361, 360-365.

Shi, Z., Tsymbalov, E., Dao, M., Suresh, S., Shapeev, A., Li, J., 2020. Deep elastic strain engineering of bandgap through machine learning (vol 116, pg 4117, 2019). *P Natl Acad Sci USA* 117, 6274-6274.

Su, M., Peng, H., Yuan, M., Li, S.F., 2021. Identification of the interfacial cohesive law parameters of FRP strips externally bonded to concrete using machine learning techniques. *Eng Fract Mech* 247.

Tvergaard, V., Hutchinson, J.W., 1996. Effect of strain-dependent cohesive zone model on predictions of crack growth resistance. *Int J Solids Struct* 33(20-22), 3297-3308.

Wisse, E., Spiering, A.J.H., van Leeuwen, E.N.M., Renken, R.A.E., Dankers, P.Y.W., Brouwer, L.A., van Luyn, M.J.A., Harmsen, M.C., Sommerdijk, N.A.J.M., Meijer, E.W., 2006. Molecular

recognition in poly(epsilon-caprolactone)-based thermoplastic elastomers. *Biomacromolecules* 7, 3385-3395.

Xu, X.P., Needleman, A., 1993. Void Nucleation by Inclusion Debonding in a Crystal Matrix. *Model Simul Mater Sc* 1, 111-132.

Yang, Z.Z., Yu, C.H., Buehler, M.J., 2021a. Deep learning model to predict complex stress and strain fields in hierarchical composites. *Sci Adv* 7, eabd7416.

Yang, Z.Z., Yu, C.H., Guo, K., Buehler, M.J., 2021b. End-to-end deep learning method to predict complete strain and stress tensors for complex hierarchical composite microstructures. *J Mech Phys Solids*, 104506.

Youssef, G., Gupta, V., 2012. Dynamic tensile strength of polyurea. *J Mater Res* 27, 494-499.

Zhang, E., Yin, M., Karniadakis, G.E., 2020. Physics-Informed Neural Networks for Nonhomogeneous Material Identification in Elasticity Imaging, p. arXiv:2009.04525.

Zhang, Z., Clifton, R.J., 2003. Shear band propagation from a crack tip. *J Mech Phys Solids* 51, 1903-1922.

Zhang, Z., Clifton, R.J., 2007. Shear band propagation from a crack tip subjected to Mode II shear wave loading. *Int J Solids Struct* 44, 1900-1926.